

FINITE-ELEMENT MODELLING OF  
THE MECHANICS OF THE COUPLING  
BETWEEN THE INCUS AND STAPES IN  
THE MIDDLE EAR

Tiong Heng Siah

A thesis submitted to the Faculty of Graduate Studies and  
Research in partial fulfilment of the requirements of the degree of  
Master of Engineering

Department of Electrical & Computer Engineering

McGill University

Montréal, Québec

March 2002

© Tiong Heng Siah, 2002



National Library  
of Canada

Acquisitions and  
Bibliographic Services

395 Wellington Street  
Ottawa ON K1A 0N4  
Canada

Bibliothèque nationale  
du Canada

Acquisitions et  
services bibliographiques

395, rue Wellington  
Ottawa ON K1A 0N4  
Canada

Your file Votre référence

Our file Notre référence

The author has granted a non-exclusive licence allowing the National Library of Canada to reproduce, loan, distribute or sell copies of this thesis in microform, paper or electronic formats.

The author retains ownership of the copyright in this thesis. Neither the thesis nor substantial extracts from it may be printed or otherwise reproduced without the author's permission.

L'auteur a accordé une licence non exclusive permettant à la Bibliothèque nationale du Canada de reproduire, prêter, distribuer ou vendre des copies de cette thèse sous la forme de microfiche/film, de reproduction sur papier ou sur format électronique.

L'auteur conserve la propriété du droit d'auteur qui protège cette thèse. Ni la thèse ni des extraits substantiels de celle-ci ne doivent être imprimés ou autrement reproduits sans son autorisation.

0-612-79096-7

Canada

## ABSTRACT

The middle ear is a small air-filled cavity which contains a chain of three small bones or ossicles: the malleus, the incus and the stapes. There is a tiny bony bridge (pedicle) between the long process of the incus and the lenticular process, but little or nothing is known about the effect of the pedicle on the movements of the ossicles. The motivation of the work presented here is to improve our understanding of the mechanical behaviour at the pedicle and the incudostapedial joint, in particular the relative contributions of the two structures to sound transmission through the middle ear.

A three-dimensional finite-element model of the pedicle and the incudostapedial joint was created, where the dimensions are based on examination of histological sections of a cat middle ear. Careful attention has been paid to the mesh generation of the model, especially for the regions of interest, such as the pedicle, that are very small relative to the overall structure. The issue of the compromise between the mesh resolution and the computational time will be discussed as well. Ranges of plausible values for the stiffnesses of the joint, joint capsule and pedicle were tested and the resulting displacements were examined for various loading conditions.

## RÉSUMÉ

L'oreille moyenne est constituée d'une petite cavité remplie d'air qui contient une chaîne de trois osselets, à savoir, le marteau (malleus), l'enclume (incus) et l'étrier (stapes). Entre le processus longus de l'enclume et le processus lenticularis se trouve une connexion osseuse très fine qui s'appelle la pédicule. Jusqu'à date nous connaissons très peu de l'effet de la pédicule sur les mouvements des osselets. Le but du présent travail est donc d'améliorer notre compréhension du comportement mécanique de la pédicule et de l'articulation incudostapédienne et plus particulièrement d'approfondir nos connaissances des contributions relatives de ces deux structures en ce qui concerne la transmission des sons par l'oreille moyenne.

Nous avons élaboré un modèle tri-dimensionnel d'éléments finis de la pédicule et de l'articulation incudostapédienne, les dimensions duquel étant basées sur l'étude de sections histologiques de l'oreille moyenne du chat. Nos efforts se sont concentrés notamment sur la génération de maillage de ce modèle, surtout par rapport aux structures, telle la pédicule, qui sont relativement minuscules. Nous discuteront aussi le compromis qu'il faut faire entre la résolution et le temps de calcul. Nous avons testé des variations des valeurs plausibles se rapportant à la rigidité de l'articulation, de la capsule d'articulation et de la pédicule, et nous avons calculé les déplacements résultant de diverses charges.

## ACKNOWLEDGEMENTS

I would like to thank my supervisor, Professor W. Robert J. Funnell, for the help he has given me in preparing this thesis, and for his guidance and patience for my English. I would also like to thank my colleagues Salim Abou Khalil, Rene G. van Wijhe and Joubin Hatamzadeh Tabrizi for their support. I would especially like to thank my colleague Qi Li, for inviting me for dinners. Finally, I am indebted to my parents, Seow Hoon and Ah Goh Siah, for their love and understanding.

This work was supported by the Canadian Institutes of Health Research and the Natural Sciences & Engineering Research Council (Canada). We thank Professor M. McKee of McGill University and S. M. Khanna of Columbia University for providing the histological sections.

# TABLE OF CONTENTS

## CHAPTER 1

<b>INTRODUCTION.....</b>	<b>1</b>
1.1 Background and Motivation .....	1
1.2 Outline.....	3

## CHAPTER 2

<b>ANATOMY OF THE MIDDLE EAR.....</b>	<b>4</b>
2.1 Human middle ear.....	4
2.1.1 Introduction.....	4
2.1.2 Eardrum.....	5
2.1.3 Ossicular chain.....	6
2.1.4 Pedicle and incudostapedial joint.....	8
2.2 Cat middle ear .....	9

## CHAPTER 3

<b>MIDDLE-EAR MECHANICS .....</b>	<b>11</b>
3.1 Impedance-matching function .....	11
3.2 Eardrum.....	12
3.3 Ossicles .....	13

## CHAPTER 4

<b>THE FINITE-ELEMENT METHOD.....</b>	<b>16</b>
4.1 Introduction.....	16
4.2 General derivation of equilibrium equations .....	16
4.2.1 Overview.....	16
4.2.2 The variational method .....	17
4.2.3 The strain-displacement matrix.....	18
4.2.4 Global finite-element equilibrium equations .....	20
4.3 Monotonic convergence.....	21

4.4 Choice of element type .....	22
<b>CHAPTER 5.....</b>	<b>25</b>
<b>MESH GENERATION .....</b>	<b>25</b>
5.1 Introduction.....	25
5.2 Mesh generators .....	25
5.2.1 TR4 .....	25
5.2.2 GRUMMP.....	27
5.2.3 GiD® .....	29
5.3 Comparison.....	30
<b>CHAPTER 6</b>	
<b>FINITE-ELEMENT MODEL .....</b>	<b>31</b>
6.1 Introduction.....	31
6.2 Pedicle-and-joint model.....	31
6.2.1 Geometry and dimensions.....	31
6.2.2 Mechanical Properties.....	34
6.2.3 Pedicle.....	35
6.2.4 Joint.....	36
6.2.5 Capsule.....	37
6.2.6 Other structures.....	38
6.3 Adequacy of mesh.....	39
6.3.1 Convergence tests .....	39
6.3.2 Reducing number of elements .....	41
6.4 Middle-ear model.....	44
6.4.1 Introduction.....	44
6.4.2 Eardrum.....	46
6.4.3 Stapedial footplate .....	46
6.4.4 Supporting ligaments .....	48
6.4.5 Modifications .....	50

6.5 Bandwidth minimization.....	56
6.6 Input stimulus.....	56

**CHAPTER 7**

<b>RESULTS .....</b>	<b>58</b>
7.1 Pedicle-and-joint model.....	58
7.1.1 Introduction.....	58
7.1.2 Base case.....	59
7.1.3 Variation of joint stiffness .....	62
7.1.4 Variation of pedicle stiffness .....	64
7.1.5 Summary .....	65
7.2 Middle-ear model.....	66
7.2.1 Introduction.....	66
7.2.2 Validation of the middle-ear model .....	66
7.2.2.1 Static displacements of the eardrum .....	66
7.2.2.2 Footplate displacements.....	68
7.2.2.3 Axis of rotation .....	71
7.2.3 Pedicle-and-joint model.....	72

**CHAPTER 8**

<b>CONCLUSION AND FUTURE WORK.....</b>	<b>77</b>
8.1 Conclusion .....	77
8.2 Future Work.....	78

<b>REFERENCES .....</b>	<b>80</b>
-------------------------	-----------

## LIST OF FIGURES

Figure 1.1	Histological section from human ear, showing the pedicle.	2
Figure 2.1	Anatomy of human middle ear.	4
Figure 2.2	Human eardrum.	5
Figure 2.3	Human ossicles.	6
Figure 2.4	Middle-ear muscles.	7
Figure 2.5	Drawing of the bony lenticular process.	8
Figure 2.6	Histological image showing the head of the stapes and the lenticular process.	9
Figure 2.7	Middle-ear anatomy of human and cat.	10
Figure 2.8	Ossicles of (a) human and (b) cat (right ear, lateral view).	10
Figure 3.1	Vibration patterns of the cat eardrum measured at (a) 4000 Hz at 117 dB SPL and (b) at 5937 Hz at 114 dB SPL.	13
Figure 4.1	Monotonic and non-monotonic convergence.	21
Figure 4.2	Collapsing an eight-node brick element into a tetrahedral element.	23
Figure 5.1	Core and ring of two consecutive 2-D contours.	26
Figure 5.2	A ‘flat’ tetrahedron is created if the boundary condition is not met.	27
Figure 5.3	Swappable configurations of five points in three dimensions.	28
Figure 5.4	Screen shot of GiD programme.	29
Figure 6.1	Shape and dimensions of the pedicle-and joint model.	32
Figure 6.2	Histological image and model of joint capsule.	33
Figure 6.3	The nature of lenticular process.	34
Figure 6.4	Histological image showing the incudostapedial joint.	37
Figure 6.5	Histological image showing the joint capsule.	38
Figure 6.6	Convergence test for the pedicle.	40
Figure 6.7	Second convergence test for the pedicle.	40
Figure 6.8	An example of stretching of a tetrahedral element.	41
Figure 6.9	An example to illustrate <i>Unstructured size transition parameter</i> in GiD.	42
Figure 6.10	Previous finite-element model of cat middle ear.	45
Figure 6.11	Finite-element model of stapes.	47
Figure 6.12	Representations of the suspending ligaments in the model.	49
Figure 6.13	Screen shots of the programme to help modifying the old finite-element model.	51

Figure 6.14	3-D reconstruction from MRI and the modified finite-element model of the middle ear.	52
Figure 6.15	3-D reconstruction from MRI and finite-element model of middle ear viewed from different perspectives.	53
Figure 6.16	The pedicle-and-joint model is incorporated into the middle-ear model.	54
Figure 6.17	Finite-element model of middle ear after including the pedicle-and-joint model.	55
Figure 6.18	Boundary condition and input stimulus of the pedicle-and-joint model.	56
Figure 7.1	The simulation results for the base case.	59
Figure 7.2	Figure defining angles $\alpha$ and $\beta$ .	60
Figure 7.3	How the angle $\beta$ is calculated.	61
Figure 7.4	The simulation results after varying the Young's moduli of the capsule and joint gap.	63
Figure 7.5	The simulation results after varying the Young's modulus of the pedicle.	64
Figure 7.6	Vibration pattern of the eardrum.	67
Figure 7.7	Finite-element model of the footplate.	68
Figure 7.8	The axis of rotation for the middle-ear model.	71
Figure 7.9	The simulation results for the pedicle-and-joint part in the middle-ear model for the base case.	72
Figure 7.10	The simulation results for the pedicle-and-joint part in the middle-ear model, for cases in which the Young's moduli of the capsule and joint gap vary.	73
Figure 7.11	The simulation results for the pedicle-and-joint part in the middle-ear model, for cases in which the Young's modulus of the pedicle varies.	74
Figure 7.12	A close-up view of the "ears".	76
Figure 8.1	More realistic pedicle and middle-ear model.	78

# CHAPTER 1

## INTRODUCTION

### 1.1 Background and Motivation

The mammalian ear can be divided into three sections: the outer ear, the middle ear, and the inner ear. The incoming acoustic signal travelling through the outer ear canal vibrates the eardrum and the pressure is then transmitted to the inner ear via the vibration of a chain of three small bones in the middle ear. Also known as ossicles, these bones can be damaged permanently by middle-ear disease, which leads to conductive hearing loss. Clinically the impaired ossicles can be replaced by middle-ear prostheses but none of these prostheses can completely restore the hearing sensitivity back to normal. In order to improve the design of the middle-ear prosthesis, it is essential to establish a better understanding of the mechanical behaviour of the middle ear. A good quantitative middle-ear model can help with that, and also lead to improvement in the development of noninvasive screening and diagnosis, especially for infants.

The three small bones forming the ossicular chain are the malleus, the incus, and the stapes. Between the long process of the incus and its extreme tip (lenticular process) is a tiny bony bridge (pedicle). Although many studies have been done on the mechanics of the ossicles, little is currently known about the function and mechanical behaviour of the pedicle. In fact, the pedicle has often been overlooked, partly because it is surrounded by soft tissue which makes it difficult to observe.

A considerable amount of experimental evidence has indicated that flexibility exists between the incus and the stapes, and it is generally believed that the flexibility originates from the incudostapedial joint. However, the pedicle's shape (see Figure 1.1) suggests that it may exhibit bending motion in normal modes of operation. If it does, then the

question arises of how much of the flexibility actually originates from the pedicle rather than from the incudostapedial joint. The objective of this research is to examine the significance of the pedicle to hearing. Potentially the work should provide some insight into the development of middle-ear prostheses.

The investigation of the bending of the pedicle is partly motivated by the earlier work that predicted bending at the manubrium of the malleus (Funnell, 1992). The recent availability of the high-resolution MRI and histological sections makes this work possible.

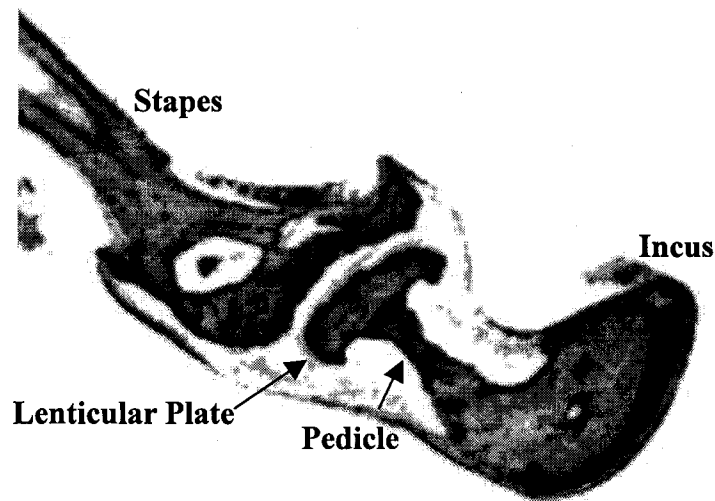


Figure 1.1: Histological section from human ear, showing the pedicle, lenticular plate and the head of the stapes.

## 1.2 Outline

In this thesis, the design and implementation of the finite-element model of the pedicle and incudostapedial joint will be described. The model has been incorporated into an existing middle-ear model to allow further investigation. Possible values for the Young's moduli of the joint, joint capsule and pedicle were tested under simple static loading conditions to study the interaction between the pedicle and the joint.

A brief overview of middle-ear anatomy and mechanics is presented in Chapter 2 and Chapter 3, respectively. Chapter 4 gives a quick review of the finite-element method; and Chapter 5 discusses the issues of mesh generation. Chapter 6 describes the implementation of the finite-element model. The simulation results are presented and discussed in Chapter 7, followed by conclusions and future work in Chapter 8.

## CHAPTER 2

### ANATOMY OF THE MIDDLE EAR

#### 2.1 Human middle ear

##### 2.1.1 Introduction

The middle ear is a small air-filled cavity which contains a linked ossicular chain, two muscles, and ligaments. As shown in Figure 2.1, the ossicular chain consists of three small bones: malleus, incus and stapes. The manubrium of the malleus is attached to the eardrum while the footplate of the stapes is connected to the oval window of the inner ear. Any incoming sound energy may vibrate the eardrum, then the ossicular chain and finally the liquid in the inner ear. The following sections in this chapter will briefly review the anatomy of the eardrum and the ossicular chain.

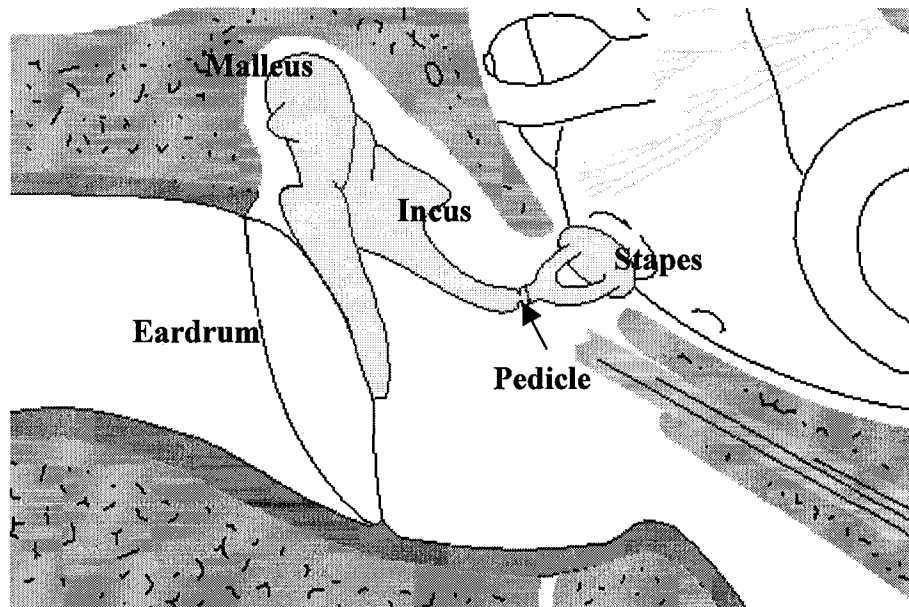
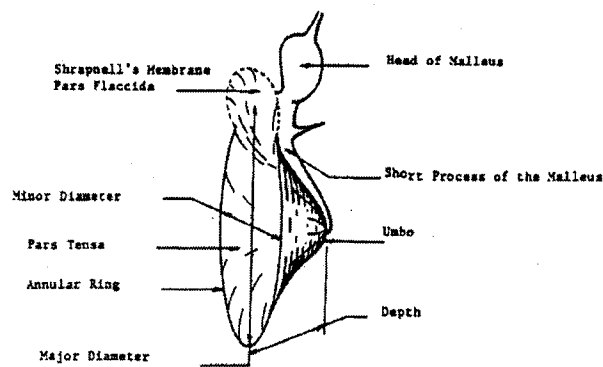


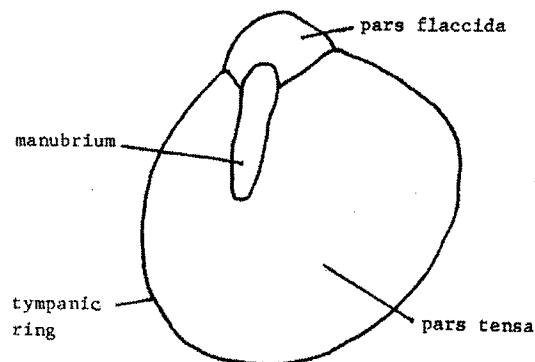
Figure 2.1: Anatomy of human middle ear.

## 2.1.2 Eardrum

The two major parts of the eardrum are the pars tensa and the pars flaccida. The pars flaccida is usually small and is more elastic than the pars tensa, and therefore it has less effect on the vibration of the eardrum. The pars tensa, on the other hand, is approximately round and conical, with the apex, which is attached to tip of the manubrium, pointing medially. The sides of the cone-shaped pars tensa are convex outward; that is clearly shown in Figure 2.2(a). Surrounding the pars tensa is an annular ligament which attaches the eardrum to the temporal bone.



(a)



(b)

Figure 2.2: The human eardrum. (a) Schematic diagram showing conical shape. From Ladak (1993), after Rabbitt (1985). (b) Outline of the eardrum showing gross anatomical regions. From Ladak (1993), after Kojo (1954).

The pars tensa is composed of three layers: 1) an outer epidermal layer; 2) the lamina propria; and 3) an inner mucosal layer. The outer epidermal and inner mucosal are continuations of the epidermis of the ear canal and the mucous lining of the middle-ear cavity, respectively. The lamina propria contains a layer of highly organized outer radial fibres and a layer of inner circular fibres. These two layers form the main structural components of the eardrum.

### 2.1.3 Ossicular chain

An illustration of the human ossicular chain is shown in Figure 2.3. The tip of the manubrium (umbo) and the lateral process of the malleus are embedded in the eardrum. The head of the malleus articulates with the body of the incus at the incudomalleolar joint. The extremity of the long process of the incus is called the lenticular plate, which forms the incudostapedial joint with the head of stapes. The head of the stapes continues to the anterior and posterior crura, which are connected to the footplate.

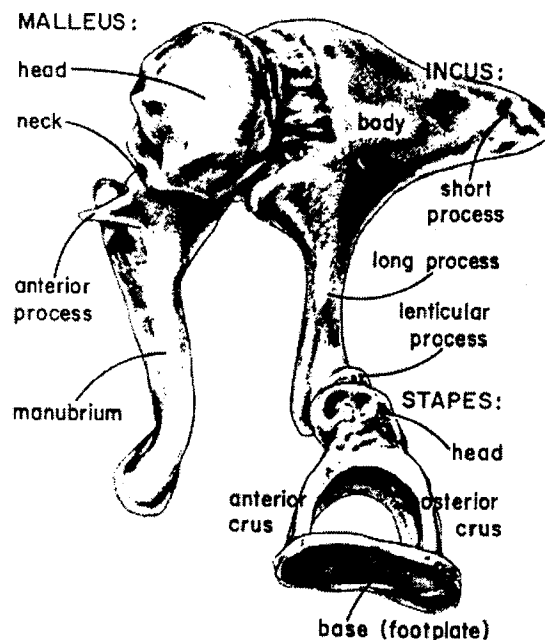


Figure 2.3: The human ossicles. From Ladak (1993), after Anson and Donaldson (1967).

There are two muscles in the middle ear, the tensor tympani muscle and the stapedius muscle. The two muscles acts as antagonist muscles, as a pull of one muscle will result in a stretching of the other (Karl-Bernd, 1996). Though both muscles help to prevent transmission of intense vibration to the inner ear, the classical theory of inner-ear protection by the acoustic reflex has been questioned. According to Prof. Harald Feldmann (Karl-Bernd, 1996), the muscles may help to maintain the circulation of the synovial fluid to the joint cartilage by their contraction.

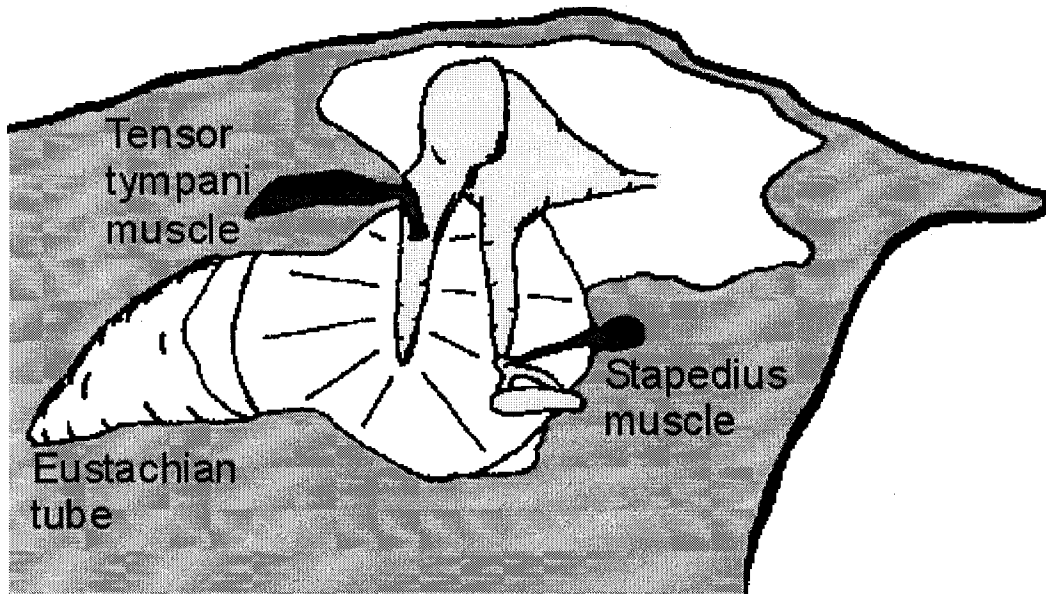


Figure 2.4: The middle-ear muscles.

### 2.1.4 Pedicle and incudostapedial joint

Between the long process of the incus and the lenticular plate is an extremely narrow pedicle. As shown in Figure 2.5, an old drawing by Shrapnell (1832), the pedicle looks like a wide supporting beam which is prone to bending. It should be noted that there are few, if any, other clear illustrations of the pedicle in the literature. As the pedicle is difficult of observe, it can easily be overlooked. Indeed, the lenticular process has occasionally been described as a separate bone, and sometimes referred to as the 'fourth ossicle' (Wolff *et al.*, 1957; Asherson, 1977; Palchun and Magomedov, 1997).

The incudostapedial joint is a synovial joint which connects the lenticular process to the head of the stapes. The articulating surfaces are lined by cartilage and are separated by a very narrow gap filled with synovial fluid. One of the major functions of the synovial fluid is to lubricate the joint, allowing the articular bones to glide smoothly. Also, both the articular bones are surrounded by a tough tissue called the joint capsule, which is responsible for providing support to the joint. Figure 2.6 shows a histological image of the incudostapedial joint and the pedicle.

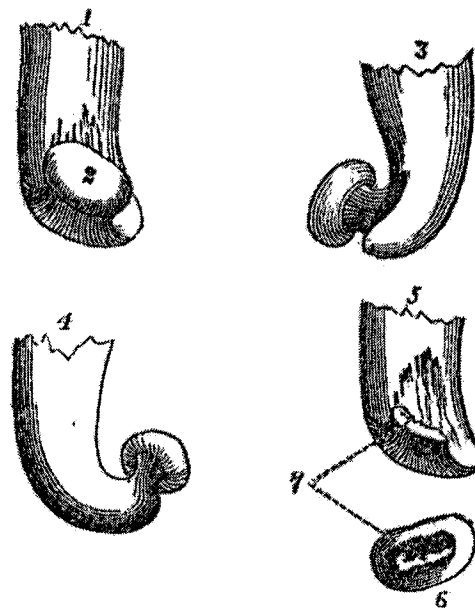


Figure 2.5: Drawing of the bony lenticular process. From Shrapnell (1832).

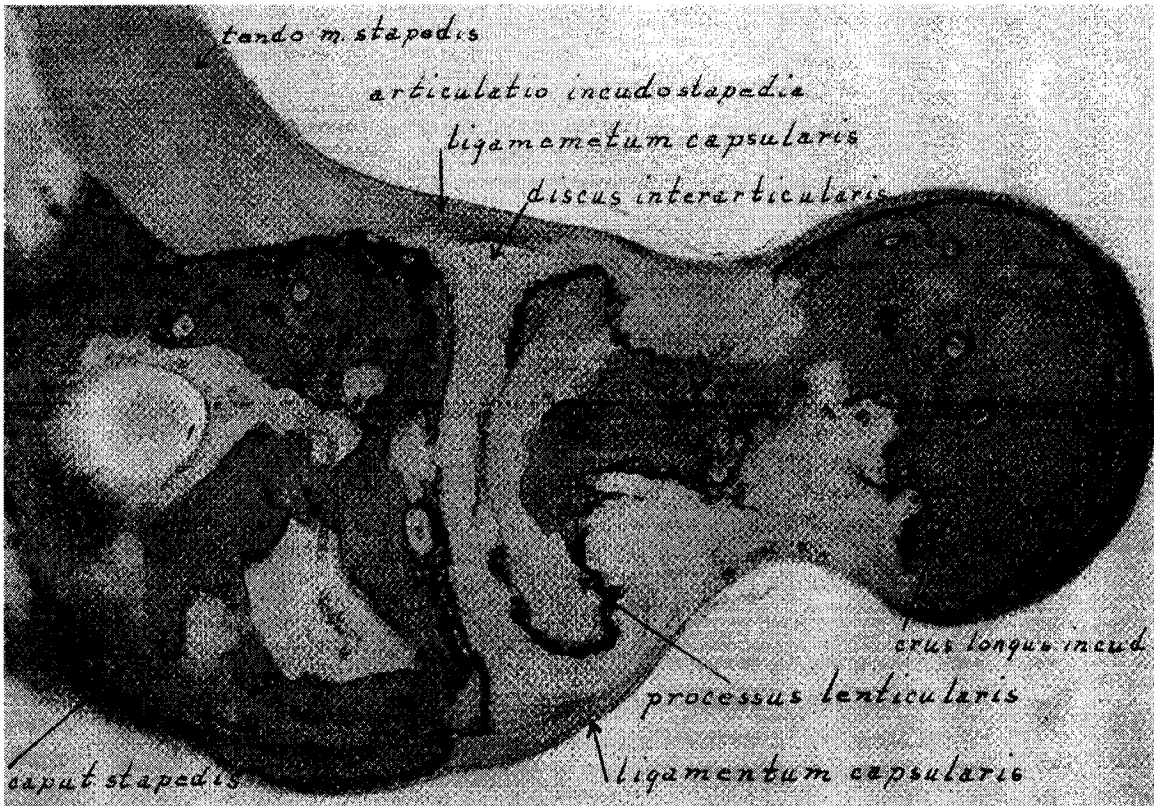


Figure 2.6: Histological image showing the head of the stapes on the left and the lenticular process on the right. From Wolff *et al.* (1957).

## 2.2 Cat middle ear

The cat middle ear is somewhat similar to the human middle ear. They both have an air-filled cavity which contains a conical eardrum and an ossicular chain, consisting of malleus, incus and stapes. They do, however, have some distinct differences in the details of the structures. For example, the middle-ear cavity of the cat has a different configuration, as illustrated in Figure 2.7. The human eardrum is roughly circular while the cat eardrum is elliptical. The ossicles of the cat and human are shown in Figure 2.8.

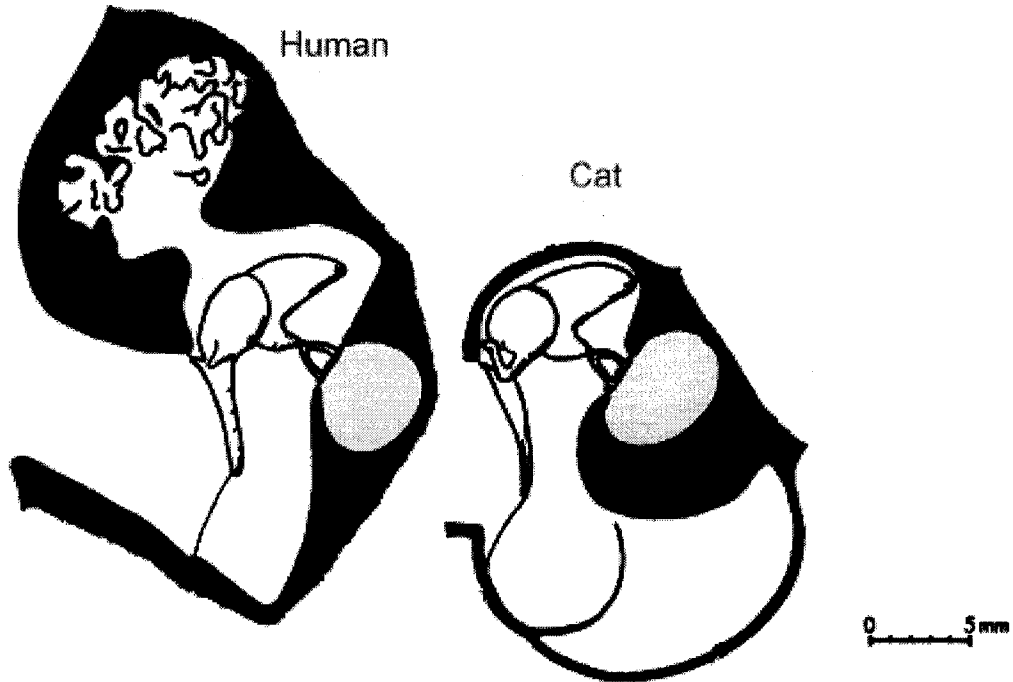


Figure 2.7: Middle-ear anatomy of human and cat. After Funnell (1972).

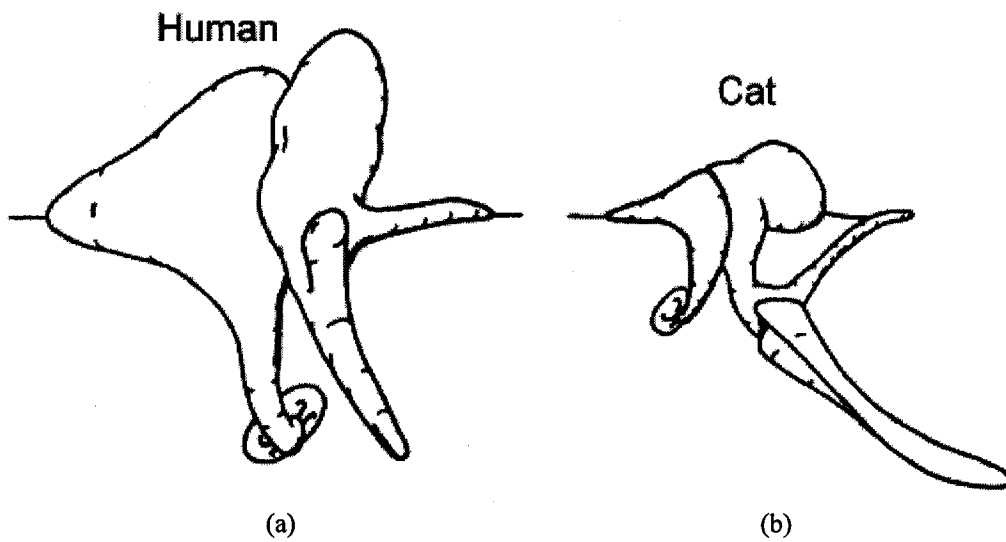


Figure 2.8: Ossicles of (a) human and (b) cat (right ear, lateral view). From Funnell (1972), (a) after Jayne (1898), (b) after Nager (1953).

## Chapter 3

### MIDDLE-EAR MECHANICS

#### 3.1 Impedance-matching function

The primary function of the middle ear is to serve as an impedance matcher between the air-filled outer ear and the liquid-filled inner ear. As the acoustic impedance of the liquid is higher than that of the air, most of the acoustic energy will be reflected if delivered directly from the air to the liquid. In the auditory system, the presence of the middle ear helps to increase the sound pressure applied to the inner ear, and hence enhances the sensitivity of hearing. This increase is obtained by: (a) the ratio of the area of the eardrum to that of the stapes footplate; (b) the lever ratio of the ossicles; and (c) the curvature of the eardrum.

The acoustic pressure applied to the eardrum produces a force which is then transferred to the stapedial footplate. Since the footplate has a smaller surface area than that of the eardrum, it exerts a greater pressure on the oval window of the inner ear. The increase of the pressure is roughly equal to the ratio of the two surface areas. For example, if the effective areas of the eardrum and the footplate are  $55 \text{ mm}^2$  and  $3.2 \text{ mm}^2$ , respectively, there will be an approximately 17 times increase of pressure at the footplate. However, the concept of a fixed area ratio implicitly requires the assumptions that the eardrum should vibrate as a stiff plate, and that the footplate should act as a piston. As seen from experimental measurements, neither assumption is true. In fact, the vibration pattern of the eardrum becomes complex at high frequencies and the displacement of the stapedial footplate is a combination of piston-like and rocking motions (Khanna and Tonndorf, 1972).

As the manubrium is longer than the long process of the incus, the malleus and incus have been described as acting as a simple mechanical lever increasing the force applied to

the footplate. Assuming a fixed axis of rotation, the increase is equal to the inverse ratio of the lengths of the lever arms. The length of the incus lever arm is given by the distance from the axis of rotation to the incudostapedial joint. The eardrum is not connected only to the umbo, however, but also at other points along the manubrium. Thus the length of the malleus lever arm should be taken as the distance from the axis of rotation to a point on the manubrium which represents the centre of action. Similar to the area ratio, the lever ratio changes with frequency. The change in the lever ratio can be caused by the shifting of the rotation axis or the flexing of the incudomalleolar joint at high frequencies.

The third mechanism of the middle-ear transformer is known as the curved-membrane effect, originally proposed by Helmholtz (1869). As discussed by Tonndorf and Khanna (1970), the curvature of the eardrum amplifies the force acting on its surface before it is applied to the manubrium (Funnell, 1996).

### **3.2 Eardrum**

As stated previously, the vibration pattern of the eardrum becomes complex at high frequencies, as illustrated in Figure 3.1. For the human eardrum, at frequencies above 2.5 kHz, the vibration pattern breaks up into independently vibrating regions which change dramatically with frequency (Khanna and Tonndorf, 1972). Similar vibration patterns have been observed using the finite-element method, which has shown a lot of success in the modelling of the eardrum since the first finite-element model of it was developed (Funnell, 1975). Yet, the greatest problem associated with the finite-element modelling is the lack of accurate measurements on the eardrum's material properties and thickness, which have a significant effect on the mechanical behaviour.

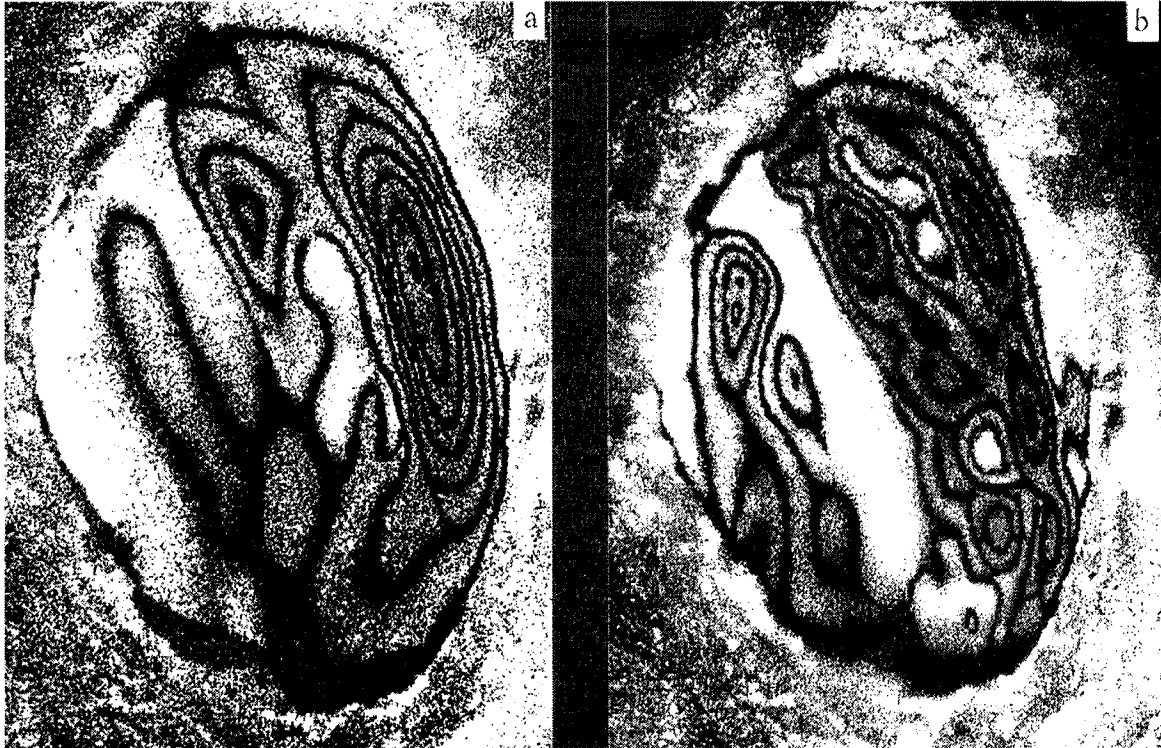


Figure 3.1: Vibration patterns of the cat eardrum measured at (a) 4000 Hz at 117 dB SPL and (b) at 5937 Hz at 114 dB SPL. After Khanna, *et al.* (1996). The vibration pattern changed dramatically when the frequency was increased from 4 KHz to about 6 KHz; there were more independently vibrating regions at the higher frequency.

Since the manubrium is coupled to different points on the eardrum, the vibration of the malleus is therefore affected by the vibrations of different parts of the eardrum (Khanna and Decraemer, 1996). Certain regions of the eardrum have been found to be ‘more effective in driving the manubrium’ (Funnell, 1996). At higher frequencies, the eardrum is poorly coupled to the manubrium (Funnell and Laszlo, 1982).

### 3.3 Ossicles

The motion of the malleus consists of both rotation and translation, and their magnitudes may vary with frequency (Decraemer *et al.*, 1991). For the rotational motion, the axis of

rotation shifts with frequency (Gundersen, 1972; Gyo *et al.*, 1987) and even within each cycle (Decraemer *et al.*, 1991). At low frequencies, where the rotation component dominates, the axis of rotation roughly matches the classical fixed rotation axis which runs from the anterior malleolar ligament to the posterior incudal ligament (Guinan and Peake, 1967).

Guinan and Peake (1967) found that, for sound pressures below 140 to 150 dB SPL (Sound Pressure Level) and for frequencies less than 3 kHz, the malleus and incus are rigidly connected by the incudomalleolar joint. At high frequencies, there is a phase difference between the malleus and the incus displacements, and that suggests some relative movement within the incudomalleolar joint.

The other joint in the middle ear is the incudostapedial joint, which has a much smaller articulating surface. Experimental observations have shown that the joint is non-rigid, as flexing at the joint has been observed (Guinan and Peake, 1967; Decraemer *et al.*, 1994). However, the effect of the pedicle was not taken into account in these observations. As a consequence, it is possible that a portion of the flexibility found between the incus and the stapes arises from the lenticular process rather than from the incudostapedial joint. The effect of the pedicle will be discussed later in Chapter 7.

The function of the flexibility of the ossicular joints is still unclear. The middle ear is always exposed to the external static (or slowly changing) air pressure, which could induce a huge (up to 1 mm) displacement of the malleus. According to Feldmann (Hüttenbrink, 1996), the gliding in the ossicular joints is therefore necessary to maintain small and piston-like displacements at the footplate.

The motion of the stapedial footplate has been studied by different researchers. It is generally accepted that the motion of the footplate is piston-like, moving in and out of the oval window (Guinan and Peake, 1967; Dankbaar, 1970; Gundersen and Hogmoen, 1976). Experimental evidence has shown that the amplitude of the footplate displacement in the z direction (towards the oval window) is ten times greater than that in

the  $x$  and  $y$  directions (in the plane of the footplate). In addition, the stapedial footplate motion involves complex rocking motions that have much smaller magnitudes (Decraemer *et al.*, 2000). According to Gyo *et al.* (1987), the stapedial footplate rocks about its longitudinal axis at low frequencies, and the motion of the stapedial footplate becomes complex at high frequencies. Decraemer *et al.* (2000) found that all 3-D components of rotation are present in the motion of stapes. At frequencies up to 8 kHz, the rotation about the long axis of the footplate dominates; and at higher frequencies, the three components of rotation become comparable.

# CHAPTER 4

## THE FINITE-ELEMENT METHOD

### 4.1 Introduction

The finite-element method is a powerful tool for solving complex structural engineering problems that involve complicated partial differential equations. The basic principle of the method is that a continuum (the total structure) is divided into subregions called *elements*, which are connected at points called *nodes*. For each element the behaviour is described by the element matrices defining the displacements in that region. The assemblage of all the element matrices forms the equilibrium equations for the continuum.

The next section will give a brief review of the derivation of the equilibrium equations. The concept of monotonic convergence will be reviewed in Section 4.3; the choice of the element type will be discussed briefly in Section 4.4.

### 4.2 General derivation of equilibrium equations

#### 4.2.1 Overview

The analysis of a system often requires the solution of the differential equations for the system. It is often very difficult, however, if not impossible, to obtain exact solutions of the governing differential equations of the system. This is particularly true if the model has irregular geometry, for instance. Therefore, approximate solution techniques have been developed and provide the basis for the finite-element method.

The variational (Rayleigh-Ritz) method and the weighted-residual method are the two most commonly used techniques (Bathe, 1982). A brief description of the variational method will be covered in Section 4.2.2.

#### 4.2.2 The variational method

The core of the method involves the principle of stationary potential energy of a system,  $\Pi$ .

$$d\Pi = \sum_{i=1}^n \frac{\partial \Pi}{\partial D_i} dD_i = 0 \quad (4.1)$$

where  $D_i$  represent the degrees of freedom (d.o.f.'s) of the  $i^{\text{th}}$  node in the system. As  $dD_i$  are independent and arbitrary, the only way for  $d\Pi=0$  is

$$\frac{\partial \Pi}{\partial D_i} = 0 \quad (4.2)$$

where  $i=1,2,\dots,n$ .

For a linearly elastic body in static equilibrium, the potential energy of the system can be expressed as

$$\begin{aligned} \Pi &= (\text{Strain Energy}) + (\text{Work Potential Of External Loads}) \\ &= U + \Omega \end{aligned} \quad (4.3)$$

The strain energy is equal to one-half the integral of strain multiplied by stress, integrated over the entire volume of the body.

$$U = \frac{1}{2} \int_V \{\varepsilon\}^T \{\sigma\} dV \quad (4.4)$$

where  $\{\varepsilon\}^T$  is the strain vector and  $\{\sigma\}$  is the stress vector.

In the constitutive equation, the relationship between stress and strain can be written in the form

$$\{\sigma\} = [C]\{\varepsilon\} \quad (4.5)$$

where  $[C]$  is a material matrix. Substituting equation (4.5) into equation (4.4) yields

$$U = \frac{1}{2} \int_V \{\varepsilon\}^T [C] \{\varepsilon\} dV \quad (4.6)$$

The potential of the loads can be expressed as

$$\Omega = - \int_V \{s\}^T \{F\} dV - \int_S \{s\}^T \{\Phi\} dS - \{s\}^T \{P\} \quad (4.7)$$

where  $\{F\}$ ,  $\{\Phi\}$  and  $\{P\}$  are the body force vector, the surface traction vector and the concentrated force vector respectively; and  $\{s\}$  is the displacement vector.

### 4.2.3 The strain-displacement matrix

Therefore, the total potential energy in one element is

$$\Pi = \frac{1}{2} \int_V \{\varepsilon\}^T [C] \{\varepsilon\} dV - \int_V \{s\}^T \{F\} dV - \int_S \{s\}^T \{\Phi\} dS - \{D\}^T \{P\} \quad (4.8)$$

It should be noted that the  $V$  and  $S$  in (4.8) correspond to the element volume and surface, respectively;  $\{s\}$  represents the element nodal displacement vector while  $\{D\}$  is the

structure nodal displacement vector. For convenience in the calculations, it is desirable to perform the integrals in a local coordinate system. The transformation between the global and local displacements is given as

$$\{s\} = [N]\{d\} \quad (4.9)$$

where  $\{s\}$  and  $\{d\}$  are vectors of global and local element displacements, respectively;  $[N]$  is a matrix of displacement interpolation functions. The corresponding element strains can be expressed as:

$$\{\varepsilon\} = [B]\{d\} \quad (4.10)$$

where  $[B]$  is the strain-displacement matrix and can be obtained by differentiating the element displacement interpolation matrix  $[N]$ . Substituting equation (4.10) into the expression for strain energy (4.6),

$$\begin{aligned} U &= \frac{1}{2} \int_V \{\varepsilon\}^T [C] \{\varepsilon\} dV = \frac{1}{2} \int_V \{[B]\{d\}\}^T [C] \{[B]\{d\}\} dV \\ &= \frac{1}{2} \int_V \{d\}^T [B]^T [C] [B] \{d\} dV \end{aligned} \quad (4.11)$$

Similarly by using equation (4.9), the potential of the loads can be rewritten as

$$\begin{aligned} \Omega &= - \int_V \{s\}^T \{F\} dV - \int_S \{s\}^T \{\Phi\} dS - \{D\}^T \{P\} \\ &= - \int_V \{d\}^T \{N\}^T \{F\} dV - \int_S \{d\}^T [N]^T \{\Phi\} dS - \{D\}^T \{P\} \end{aligned} \quad (4.12)$$

#### 4.2.4 Global finite-element equilibrium equations

Hence the total potential energy in the system, with  $M$  elements, is a sum of the potential energies of all finite elements,

$$\Pi = \frac{1}{2} \sum_{i=1}^M \{d\}_i^T [k]_i \{d\}_i - \sum_{i=1}^M \{d\}_i^T \{r\}_i - \{D\}^T \{P\} \quad (4.13)$$

where

$$[k]_i = \int_{V_i} [B]^T [C]_i [B] dV \quad (4.14)$$

is the element stiffness matrix for element  $i$ , and

$$\{r\}_i = \int_{V_i} [N]^T \{F\} dV + \int_{S_i} [N]^T \{\Phi\} dS \quad (4.15)$$

is the element load vector. Equation (4.13) can be rewritten by replacing  $\sum \{d\}$  by  $\{D\}$ ,

$$\Pi = \frac{1}{2} \{D\}^T [K] \{D\} - \{D\}^T \{R\} \quad (4.16)$$

where

$$[K] = \sum_{i=1}^M [k]_i \quad \text{and} \quad \{R\} = \{P\} + \sum_{i=1}^M \{r\}_i \quad (4.17)$$

Equation (4.16) may be differentiated with respect to each nodal displacement variable in order to obtain the finite-element equilibrium equations as

$$[K] \{D\} = \{R\} \quad (4.18)$$

Equation (4.18) applies only to the static (or low frequency) case, in which the effect of inertia and damping are ignored. For a high-frequency dynamic analysis, the finite-element equilibrium equations can be expressed as

$$[K]\{D\} + [C]\{D\}' + [M]\{D\}'' = \{R\} \quad (4.19)$$

where  $[C]$  and  $[M]$  represent the damping matrix and the mass matrix, respectively;  $\{D\}'$  and  $\{D\}''$  are the first and second time derivatives of the displacement matrix, respectively. Detailed descriptions of equation (4.19) can be found in many finite-element reference books and will not be covered here.

### 4.3 Monotonic convergence

The concept of monotonic convergence can be illustrated by Figure 4.1. As shown in the graph, the dashed monotonic convergence line approaches the exact solution on each successive mesh refinement. One of the advantages of this behaviour is that a more precise solution is always guaranteed as the number of finite element increases.

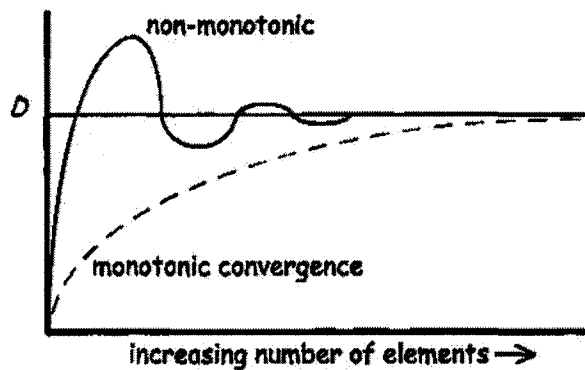


Figure 4.1: Monotonic and non-monotonic convergence. For monotonic convergence, the solution of the analysis approaches the exact solution  $D$  as the number of elements increases.

To ensure monotonic convergence, the elements must be *complete* and *compatible*. The completeness of an element means that the displacement function must be able to account

displacements of the element without straining. Constant-strain states indicate that the strain in each individual element must approach a constant strain as the element size becomes very small. The compatibility means that the displacements within the elements and across the element boundaries must be continuous. In another words, no gaps or overlaps are allowed between elements before or after the analysis.

#### 4.4 Choice of element type

There is a variety of element types that can be employed for finite-element analysis. The basic element can be as simple as a 2-node line or as complex as a 20-node hexahedral element. The considerations for the element type normally involve the accuracy of solution, computer resources required and the geometry of the model. In the analysis presented in this thesis, the tetrahedron has been selected to be the basic three-dimensional element as it could theoretically be used to model any solid structure.

An example of a generalized material matrix [C] for isotropic materials for a three-dimensional element is shown here:

$$C = \frac{E(1-\nu)}{(1+\nu)(1-2\nu)} \begin{bmatrix} 1 & \frac{\nu}{1-\nu} & \frac{\nu}{1-\nu} & 0 & 0 & 0 \\ \frac{\nu}{1-\nu} & 1 & \frac{\nu}{1-\nu} & 0 & 0 & 0 \\ \frac{\nu}{1-\nu} & \frac{\nu}{1-\nu} & 1 & 0 & 0 & 0 \\ 0 & 0 & 0 & \frac{1-2\nu}{2(1-\nu)} & 0 & 0 \\ 0 & 0 & 0 & 0 & \frac{1-2\nu}{2(1-\nu)} & 0 \\ 0 & 0 & 0 & 0 & 0 & \frac{1-2\nu}{2(1-\nu)} \end{bmatrix} \quad (4.20)$$

where  $E$  is the material modulus of elasticity (Young's modulus) and  $\nu$  is the Poisson's ratio.

The finite-element analysis program SAP IV used in the laboratory does not truly support tetrahedral elements. One possible trick that can be used is to collapse the eight-node brick element supported by SAP IV to a four-node tetrahedral element, as demonstrated in Figure 4.2.

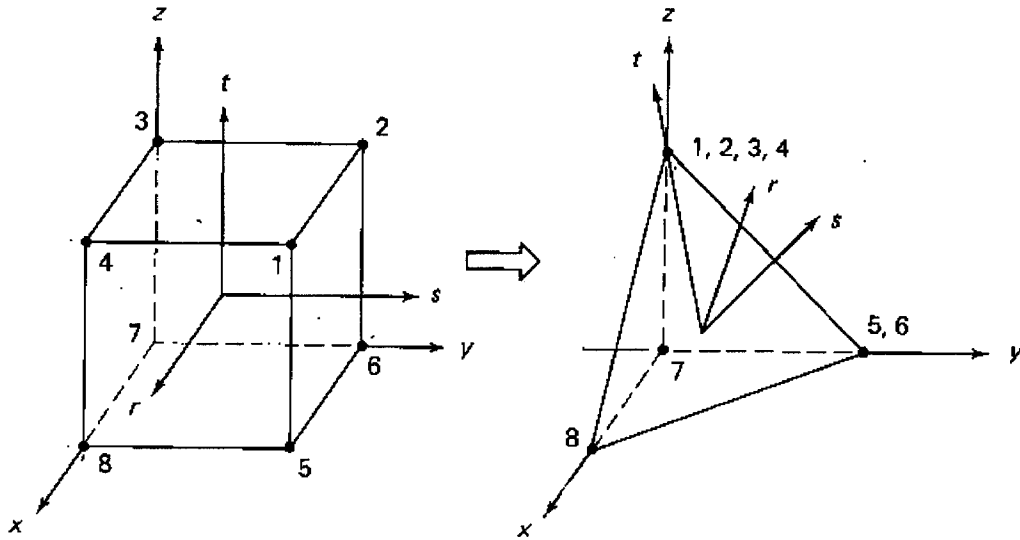


Figure 4.2: Collapsing an eight-node brick element into a tetrahedral element

As mentioned in the Master's thesis of S. Funnell (1989), modifications have to be made to the code to remove the addition of incompatible modes to the brick element. The incompatible modes are added to the brick element to reduce the analysis cost and speed up the convergence rate. The improvement is achieved by adding higher-order displacement interpolation to represent a constant bending moment. For example,

$$\begin{aligned}
u &= \sum_{i=1}^8 h_i u_i + \alpha_2(1-r^2) + \alpha_2(1-s^2) + \alpha_3(1-t^2) \\
v &= \sum_{i=1}^8 h_i v_i + \beta_2(1-r^2) + \beta_2(1-s^2) + \beta_3(1-t^2) \\
w &= \sum_{i=1}^8 h_i w_i + \gamma_2(1-r^2) + \gamma_2(1-s^2) + \gamma_3(1-t^2)
\end{aligned}$$

$\uparrow \qquad \qquad \uparrow \qquad \qquad \uparrow$   
*incompatible modes*

This is generally advantageous provided the elements are not badly distorted, which is not the case for the collapsed-brick tetrahedral elements. As a result, the modified code, written by S. Funnell (1989), is used here for finite-element analysis.

# CHAPTER 5

## MESH GENERATION

### 5.1 Introduction

Mesh generation is one of the most crucial parts in the finite-element analysis and it is definitely not a trivial task. Numerous algorithms have been developed and yet mesh generation is still an ongoing challenge.

Section 5.2 briefly reviews three potential tetrahedral mesh generators: TR4, GRUMMP and GiD; Section 5.3 compares the three mesh generators in terms of their performance and capabilities.

### 5.2 Mesh generators

#### 5.2.1 TR4

TR4 is a 3-D mesh generator originally developed by Boubez (1986), a Master's student in the laboratory. The programme was intended to work alongside Fie, a programme developed locally for *segmentation*, to construct 3-D biological models. It should be noted that segmentation is a process of specifying the boundaries of regions of interest from image sources, such as MRI and histological data. Briefly speaking, the segmentation programme Fie defines the boundaries of the model and, based on that, TR4 generates the mesh. The capabilities of TR4 were further improved by S.M. Funnell (1989), a Master's student in the laboratory, to handle more general irregularly shaped objects.

The main philosophy of the algorithm is to construct 3-D meshes between every two adjacent slices of contours, and assemble all the meshes to complete the whole volume

mesh. Basically the programme divides the volume between slices into two parts: the *core* and the *ring*, which are dealt with separately. The core is first divided evenly into triangular prisms and then each prism is divided into six tetrahedra. The mesh generation for the ring is much more complicated. It should be noted that no additional nodes are generated during the meshing process, and that is quite different from most of the mesh generators available. Figure 5.1 shows an example of a 3-D *core* and *ring* of two consecutive 2-D contours.

Sometimes it is possible to reach a situation where the ring cannot be divided into tetrahedra without modifying its surface triangulation. That, however, would make it incompatible to the surface triangulations of the core. The idea of a “flat” tetrahedron is proposed to preserve the compatibility (see Figure 5.2). The “flat” tetrahedron will be inflated by relaxation afterward. More detailed descriptions of the TR4 programme can be found in the Master’s theses of Boubez (1986) and Funnell (1989).

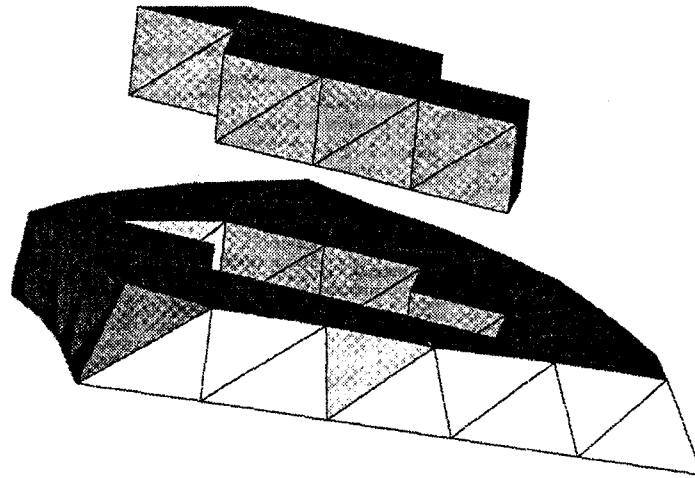
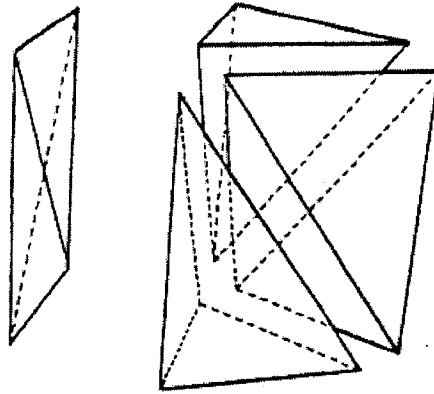


Figure 5.1: Core and ring of two consecutive 2-D contours. After Funnell (1989)



(b)

Figure 5.2: A 'flat' tetrahedron is created in order to preserve compatibility between the surface triangulations of the core and the ring. After Funnell (1989)

### 5.2.2 GRUMMP

GRUMMP (Generation and Refinement of Unstructured, Mixed-Element Meshes in Parallel) is a freely distributed mesh generator. The programme is capable of generating high-quality 2-D and 3-D meshes. It features sophisticated mesh improvement functions to reduce poorly shaped elements that can possibly cause numerical problem.

GRUMMP is essentially a Delaunay-based generator. Therefore, the constructed mesh of tetrahedra has to satisfy the *Delaunay criterion* that the circumsphere defined by each tetrahedron contains no mesh nodes in its interior. However, employing the Delaunay criterion alone is not sufficient to avoid poorly shaped tetrahedra. Additionally, it does not guarantee that the mesh nodes lie within the bounding surfaces. As a result, additional refinement techniques are usually used to enhance the performance (Yuan and Fitzsimons, 1993 and Shewchuk, 1998)

In GRUMMP, improvement mechanisms adopted include *face swapping* and a modified *Laplacian smoothing method* (Ollivier-Gooch, 1998). Face swapping is a very common technique which changes the local connectivity so as to improve the mesh quality. For example, there are two legal configurations to divide the structure shown in Figure 5.3 into tetrahedra. The objective of the face-swapping algorithm is to select the most appropriate configuration which minimizes the *maximum dihedral angle* (angle between two facets of the tetrahedron) and satisfies the Delaunay criterion. The Laplacian smoothing method is an operation that optimizes the location of each vertex according to its neighbours. The smoothing method implemented in GRUMMP is claimed to be *smarter*, as it only accepts a change in vertex location if that can lead to improved mesh quality.

It has been shown that the combination of the swapping followed by the smoothing technique yields better improvement than applying each mechanism individually (Freitag and Ollivier-Gooch, 1997). More information about GRUMMP can be found at <http://tetra.mech.ubc.ca/GRUMMP/>.

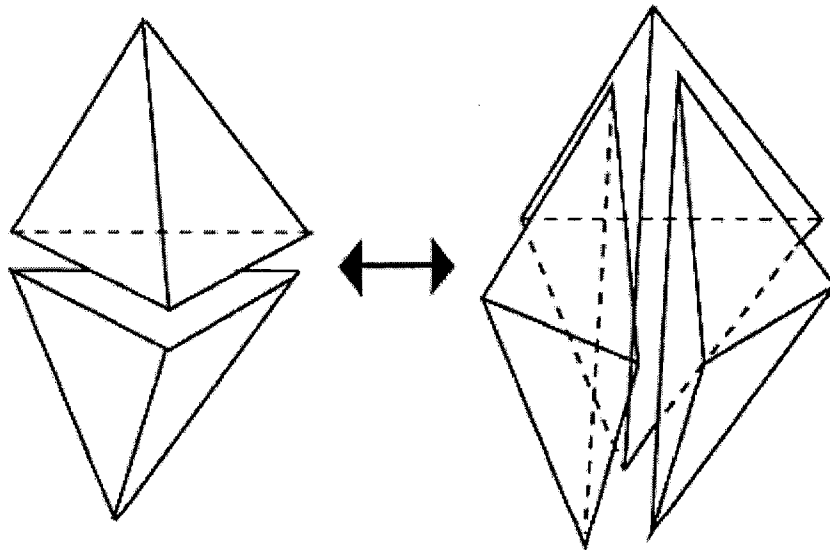


Figure 5.3: Swappable configurations of five points in three dimensions. There are two ways to divide the structure into tetrahedra. The configuration on the left is preferable and that can be determined by selecting the one with the smallest maximum dihedral angle. After Freitag and Ollivier-Gooch (1997).

### 5.2.3 GiD<sup>®</sup>

GiD is a general-purpose pre-postprocessor for finite-element analysis. It adopts the *advancing-front technique*, another popular algorithm for mesh generation. Descriptions of the software can be found at <http://gid.cimne.upc.es>.

One main problem associated with the traditional Delaunay-based algorithms is that special care has to be taken to remove elements that lie outside the domain, or cross the boundary. However, this is not a problem for the advancing-front algorithm. The method operates by first triangulating the surfaces to create an initial front, and then moving forward to connect each triangle segment to a fourth node to form a tetrahedron. The tetrahedron will then be removed and the remaining triangular faces will form the new fronts. The process will continue until the whole volume is meshed with tetrahedral elements. As the mesh is initiated from the boundary surfaces, the problem of the elements lying outside the boundary, that may occur in the Delaunay triangulation, is avoided (George and Seveno, 1994; Moller and Hansbo, 1995).

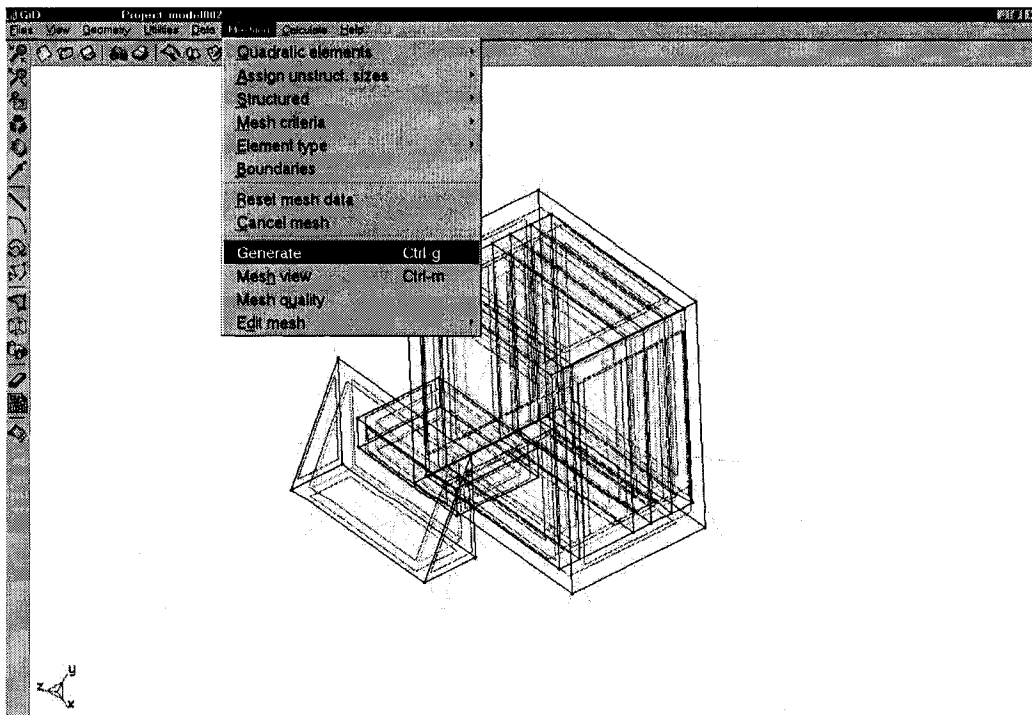


Figure 5.4: Screen shot of GiD programme. User is about to start the mesh generation process.

### 5.3 Comparison

Table 5.1 shows a comparison for the three mesh generators. In selecting a suitable mesh generator, the major consideration is definitely the capability to generate a tetrahedral mesh on irregularly shaped structures with a high success rate. GiD simply tops the other two in this category as both TR4 and GRUMMP may occasionally fail in generating the mesh. In addition, GiD offers the possibility of creating non-uniform meshes, which is helpful in reducing the total number of elements. The programme also comes with a visualisation tool that has been used extensively in this work to display the finite-element models and simulation results. A major drawback, however, is that its source code is not available. In conclusion, GiD has been selected as the best choice among the three.

	<b>TR4</b>	<b>GRUMMP</b>	<b>GiD</b>
<b>Support Tetrahedral Element</b>	Yes	Yes	Yes
<b>Control Over Element size</b>	Yes	Yes	Yes
<b>Support Non-uniform Mesh</b>	No	No	Yes
<b>Mesh Refinement</b>	<i>Smoothing</i>	<i>Face swapping, Laplacian smoothing</i>	<i>N.A.</i>
<b>Customizable Output</b>	Yes	Yes	No
<b>Built-in Visualisation Tool</b>	No	No	Yes
<b>Friendly Interface</b>	No	No	Yes
<b>Source Code Available</b>	Yes	Yes	No
<b>Free</b>	Yes	Yes	No
<b>Technical Support</b>	<i>Local</i>	Yes	Yes
<b>Remarks</b>	<i>Fails sometimes</i>	<i>Fails sometimes</i>	<i>Always works</i>

Table 5.1: Comparison of TR4, GRUMMP and GiD

## Chapter 6

# FINITE-ELEMENT MODEL

### 6.1 Introduction

This chapter begins with a description of the modelling of the pedicle and the incudostapedial joint. The pedicle-and-joint finite-element model is presented in Sections 6.2 and 6.3. The pedicle-and-joint model was tested within an existing model of the complete middle ear. Section 6.4 gives a brief description of the complete middle-ear model.

### 6.2 Pedicle-and-joint model

#### 6.2.1 *Geometry and dimensions*

The pedicle-and-joint model is a simplified representation of the true anatomy, and therefore the implementation and the modification, if necessary, of the model can be accomplished more easily than for a realistic model. The modelling of the simple model as well as the preliminary simulation results should provide some insight into the development of a more realistic model in the future. Figure 6.1(a) and (b) show histological images of a cat middle ear. As shown in Figure 6.1(c) and (d), the model consists of the end of the long process of the incus, the pedicle, the lenticular plate, the joint gap, the joint capsule, and the head of the stapes. The dimensions of each structure were approximated based on histological sections of a cat middle ear. Figure 6.1(e) and (f) show the model's dimensions that are based on histological sections as shown in Figure 6.1(a) and (b). Despite the fact that the simple model could easily be meshed with brick elements, tetrahedral elements are used here because the experience with tetrahedral elements will help with future work on a more realistic model. Chapter 8 will review the issue of the realistic model in greater detail.

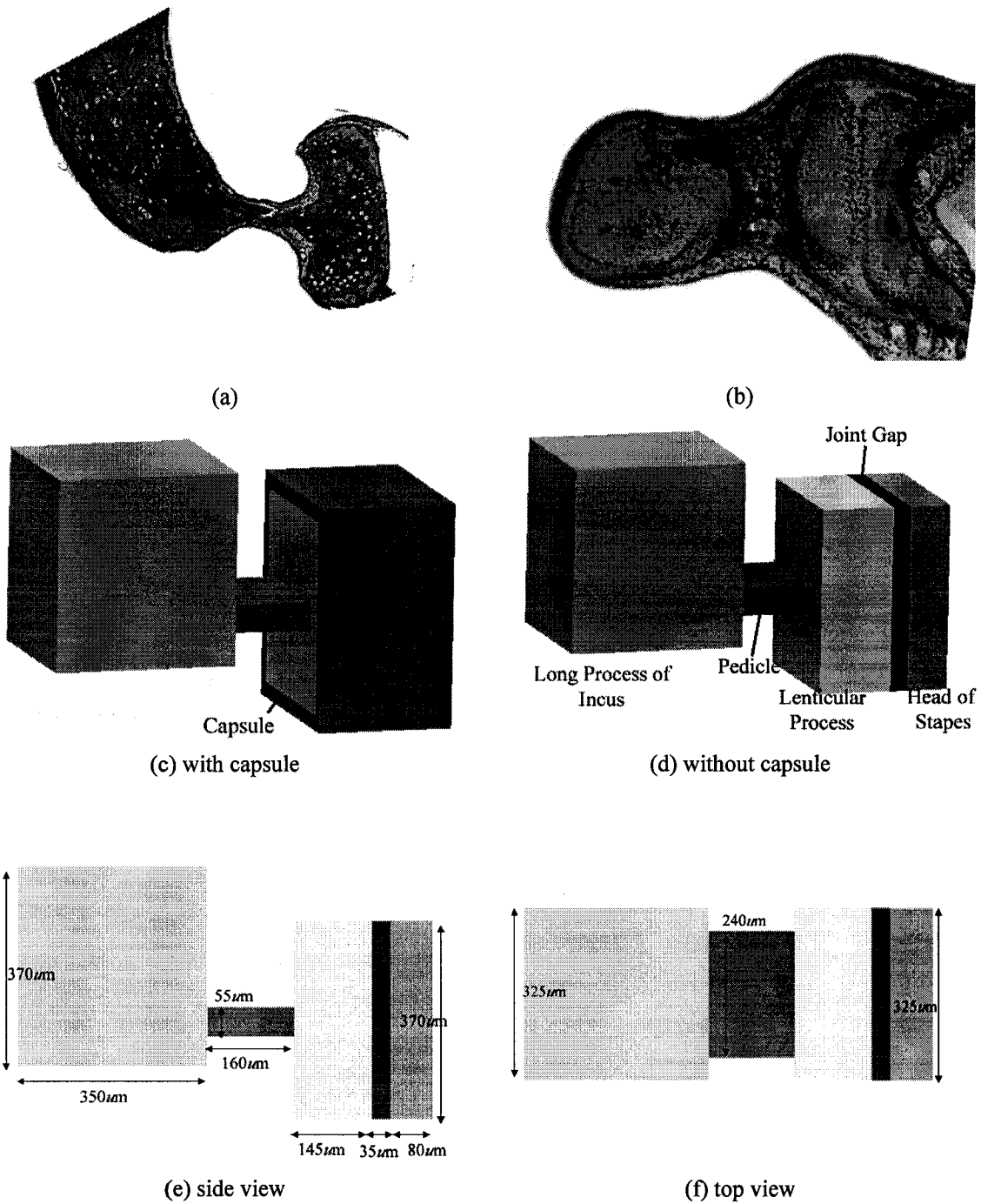
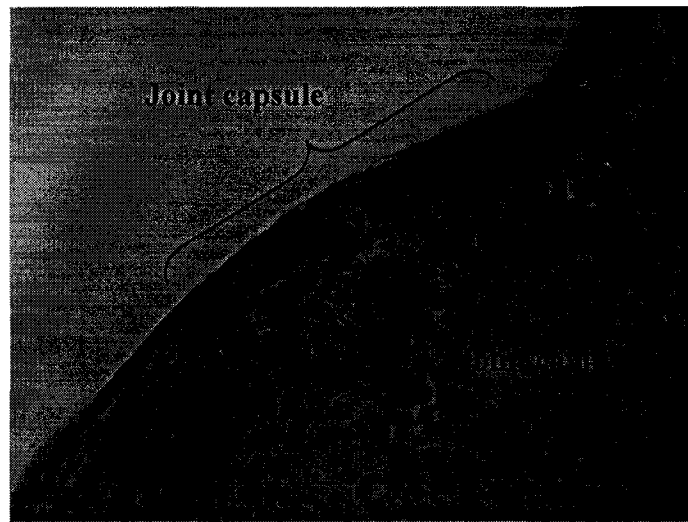
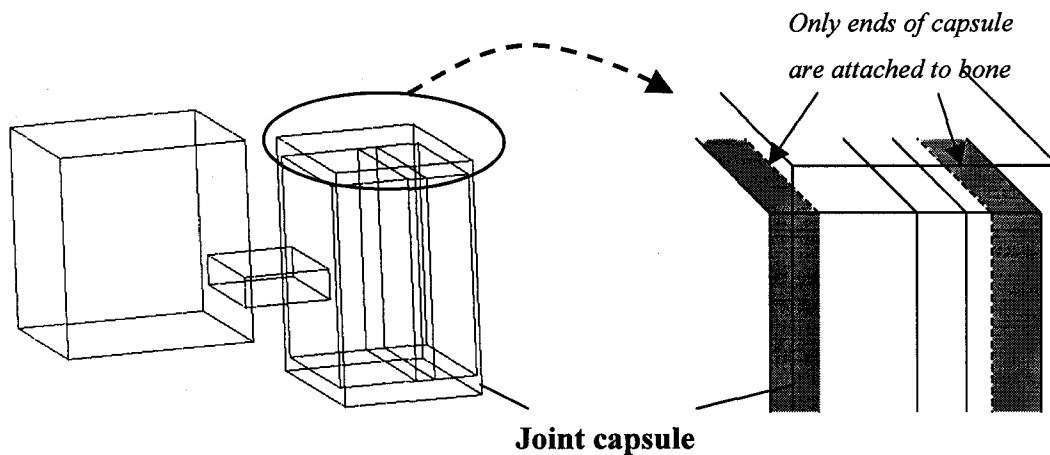


Figure 6.1: (a) is one of the 1- $\mu$ m-thick histological serial sections, stained with toluidene blue, received 2001 Jan from M. McKee (Dept. Anatomy & Cell Biology, McGill University). (b) is one of the 50- $\mu$ m-thick histological serial sections, stained with Hematoxylin and Eosin (H&E), provided by Khanna. Geometry(c)(d) and dimensions (e)(f) of the pedicle-and-joint model are determined based on histological sections (a)(b).

The pedicle is modelled by a  $55\ \mu\text{m} \times 160\ \mu\text{m} \times 240\ \mu\text{m}$  beam. The joint cavity or gap in the incudostapedial joint is represented by a  $35\text{-}\mu\text{m}$ -thick articular cartilage as discussed in Section 6.2.4. Surrounding the joint is a  $30\text{-}\mu\text{m}$ -thick layer representing the joint capsule. To be consistent with the real anatomy of the joint capsule as observed in the histological sections, only the two ends of the capsule are attached to the bone (see Figure 6.2).



(a)



(b)

Figure 6.2: (a) Histology of joint capsule (H&E). It should be noted that only the ends of the joint capsule are attached to the bone, and it has been taken into consideration when building the finite-element model as illustrated in (b).

## 6.2.2 Mechanical Properties

The material properties of the model are assumed to be linear, uniform (i.e., the same in all locations) and isotropic (i.e., the same in all directions). The assumption of linearity is generally valid in the middle ear under normal hearing conditions. At low frequencies at which the effects of damping and inertia are negligible, the material properties of a linear isotropic structure can be completely described by its Young's modulus (Pa or  $\text{N/m}^2$ ), and Poisson's ratio, a dimensionless number.

Poisson's ratio for all materials has been taken to be 0.3. Explicit sensitivity tests suggest that varying the Poisson's ratio has little effect on the simulation results of the model, which matches the earlier findings by Funnell (1975). The tests indicate that mechanical behaviour of the middle ear is primarily determined by its stiffness and the Poisson's ratio is found to be less important.

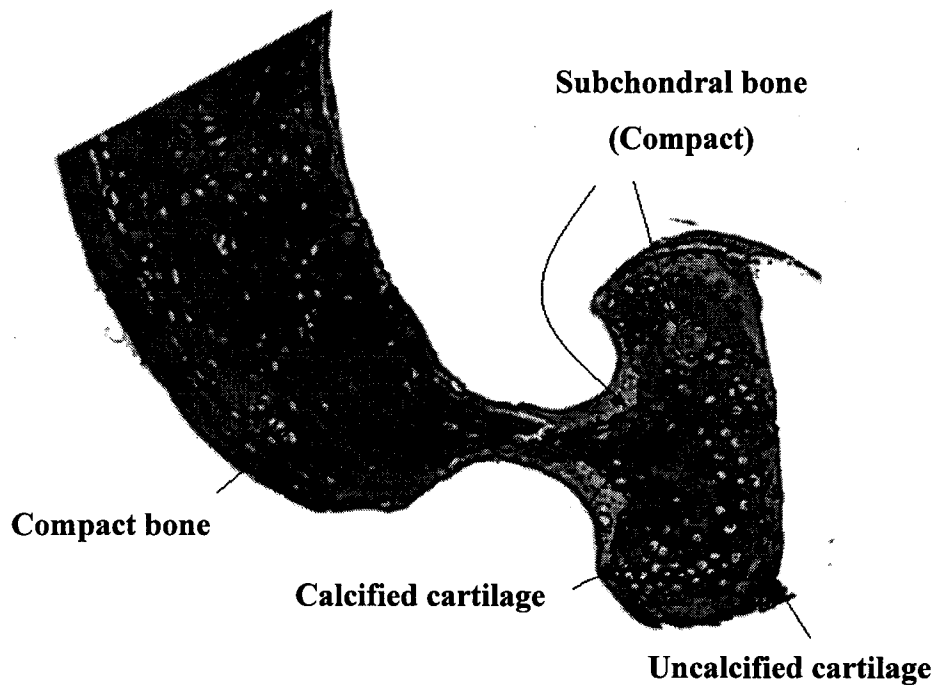


Figure 6.3: The nature of lenticular process.

As mentioned in the previous chapter, the work presented here has been made possible by the availability of highly detailed histological sections which show the precise nature of the pedicle and the incudostapedial joint. With the help of M. McKee, Professor in the Department of Anatomy & Cell Biology of McGill University, the nature of the material types has been identified, as illustrated in Figure 6.3.

Calcified cartilage is a cartilage layer close to bone and is about ten times stiffer than uncalcified cartilage. Most of the lenticular plate is calcified cartilage. The articulating surface of the lenticular plate is a thin layer of uncalcified cartilage, which stains lighter. Subchondral bone can be defined as a bone layer just beneath the cartilage, and it serves as a cushion between the calcified cartilage and the stiffer compact bone. There are regions of subchondral bone in the lenticular plate. The long process of the incus consists mainly of compact bone.

The determination of the material properties of living tissues is not easy, because they can vary widely, depending on their location, direction of measurement, etc. Sections 6.2.3 to 6.2.6 discuss the material properties of the structures in the pedicle-and-joint model.

### *6.2.3 Pedicle*

Evidence from the serial histological sections suggests that the pedicle is a continuation of bone from the long process of the incus to the lenticular plate. The Young's modulus for bone varies from 1 G to 27 GPa, depending on the nature of the bone, the direction of measurement, and the part of the bone.

In estimating the stiffness of the pedicle, the work done by Mente and Lewis (1994) is particularly useful because the measurements were conducted on small bone specimens obtained beneath joint cartilage. As mentioned before, this type of bone is sometimes referred to as subchondral bone. Since the pedicle is very close to the joint cartilage, it

can be considered as subchondral bone, and therefore a Young's modulus of 5 GPa (Mente and Lewis, 1994) is adopted for the pedicle.

On the other hand, histological evidence suggests that the pedicle could actually be a single *osteon*, the principal organizing feature of compact bone. For a single osteon, the Young's modulus was calculated to be 10.7 GPa by Ascenzi (1967). A modulus of 21.7 GPa was calculated by Rho *et al.* (1998), but the value could have been overestimated, as the bone specimens used were dehydrated, which can lead to an increase in stiffness (Elices, 2000). Therefore, the simulations also include cases in which a Young's modulus of 12 GPa is used for the pedicle.

#### 6.2.4 Joint

The incudostapedial joint is a synovial joint, in which the load is transferred from a cartilage layer on one bone to a cartilage layer on the other bone, either through direct contact, or through a thin film of synovial fluid between the cartilage layers, or by a mixture of both. Examination of the histological images shows that the thickness between the two articulating surfaces is so small that the cartilage on both sides is probably (at least partially) in direct contact during acoustic vibration. Therefore, the contacting region in the joint has been modelled as a single block of articular cartilage (ignoring the synovial fluid space), which has a Young's modulus of around 10 MPa as measured in normal human articular cartilage (Elices, 2000).

The synovial fluid functions as a lubricant which allows the two articulating surfaces to glide easily. It should be noted that the modelling of the thin film of synovial fluid would be technically complicated. Limited by the finite-element programme SAP IV used in the laboratory, the sliding contact surface is not implemented in this model. This implies that the two articulating surfaces in the model are firmly attached and the three components of the stress are transferred, with no loss, from one surface to another in the

joint. In reality, the stress parallel to the articulating surface will possibly be greatly attenuated because of the synovial fluid. As a consequence, the in-plane displacements of the footplate may be smaller than those predicted by the simulation results.



Figure 6.4: Histology showing the incudostapedial joint. Between the two articulating surfaces is an extremely narrow gap, filled with synovial fluid (arrow).

### 6.2.5 Capsule

Another key structure in the model is the incudostapedial joint capsule that completely encloses the joint. The outer layers of the capsule consist of dense fibrous connective tissue, the capsule ligament, which dominates the capsule mechanical properties. It is therefore reasonable to apply the value of Young's modulus for capsule ligament to the capsule directly. Hewitt and Guilak (2000) reported that the Young's moduli for the hip joint capsules range from 76.1 to 285.8 MPa. Itoi *et al.* (1993) calculated the Young's modulus for the shoulder joint capsule to be in the range from  $31.5 \pm 9.4$  MPa to  $66.9 \pm 9.4$  MPa. In fact, "the overall material behavior properties of the ligaments of different joint capsules are similar but not identical" (Hewitt and Guilak, 2000).

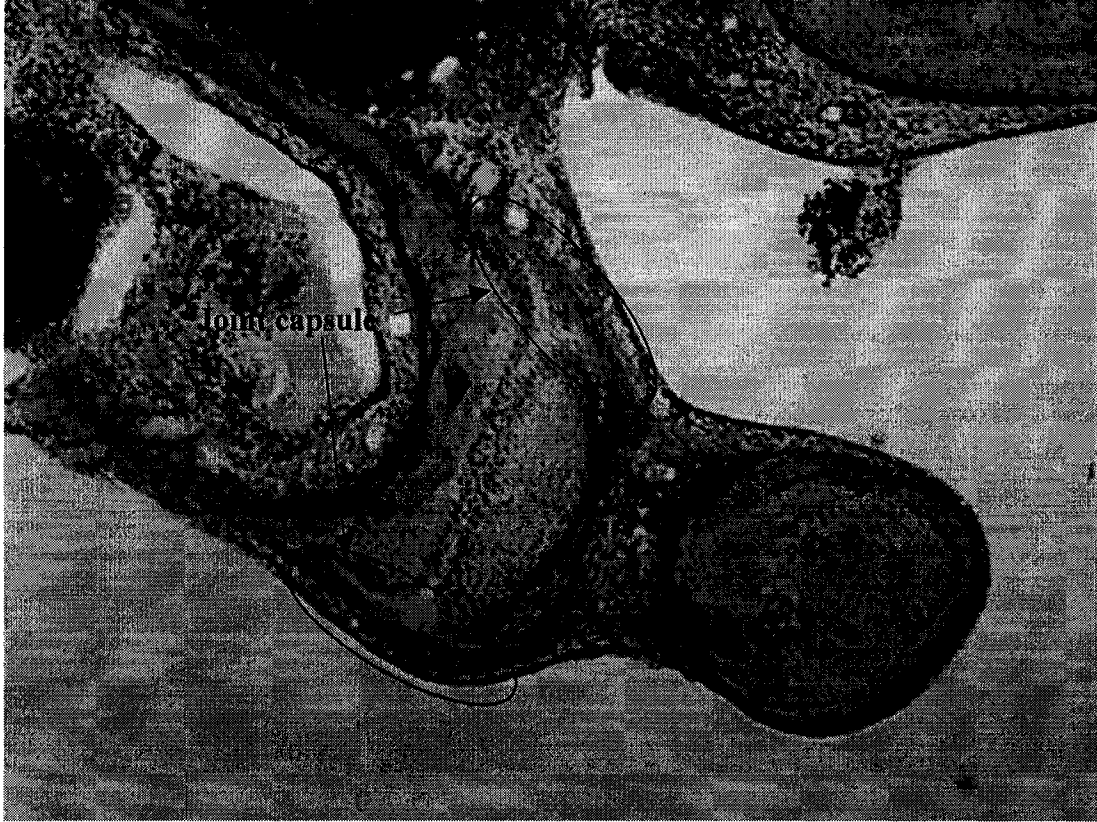


Figure 6.5: Histology showing the joint capsule

Since it is not clear what the Young's modulus of the incudostapedial joint capsule should be, possible values such as 20 MPa, 50 MPa and 100 MPa are used in the simulations discussed in the next chapter.

### 6.2.6 Other structures

The long process of the incus is given a Young's modulus of 12 GPa, corresponding to stiff compact bone. Since the long process of the incus is so wide that it will bend little, the exact value of its Young's modulus is unimportant.

The lenticular plate and the head of the stapes consist partly of calcified cartilage and partly of subchondral bone, and their Young's moduli are 0.3 GPa and 5 GPa,

respectively (Mente and Lewis, 1994). Hence an intermediate value of 1 GPa is used as the Young's modulus for the two structures.

## **6.3 Adequacy of mesh**

### **6.3.1 Convergence tests**

In general the accuracy of a finite-element analysis increases with the mesh resolution. On the other hand, the computation time of the analysis is more than linearly proportional to the number of nodes. Hence, one important question that needs to be addressed here is how many elements are enough for accurate simulation results while keeping reasonable computation time. In order to determine a suitable mesh resolution, most of the major substructures in the model were tested in simple convergence tests that involved both compressive and shearing loads. An optimal resolution was then decided upon for each substructure.

An example of a convergence test for the pedicle is shown in Figure 6.6, in which the maximum displacement is plotted as a function of the number of elements. A  $y$ -direction shearing force was applied uniformly to one face while the opposite face was clamped. The mesh is uniform and isotropic, and constituted of tetrahedral elements. In this case, a mesh with 2000 elements is fine enough for the simulation results to converge (within ~ 5%) to the analytical results.

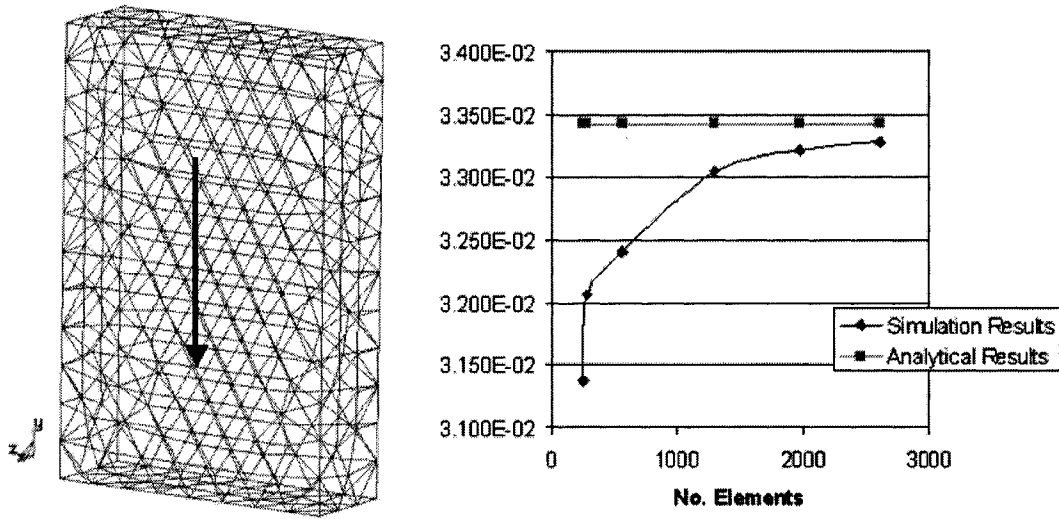


Figure 6.6: Convergence test for the pedicle. A  $y$ -component shearing load was applied on one face while the opposite face was clamped. A mesh resolution with at least 2000 elements is required for high accuracy in this case.

Figure 6.7 shows another convergence test for the pedicle; the shearing load was applied in the  $x$  direction in this case. Clearly a mesh with only 2000 elements is not even close to reaching the plateau region of the curve, and a mesh with at least 10000 elements should be used if the desired discrepancy is less than 5%.

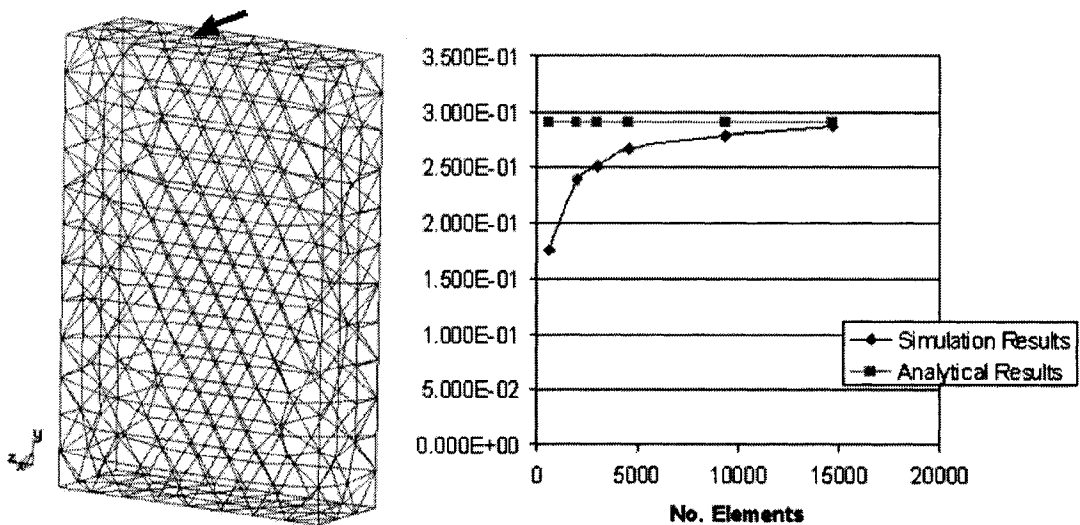


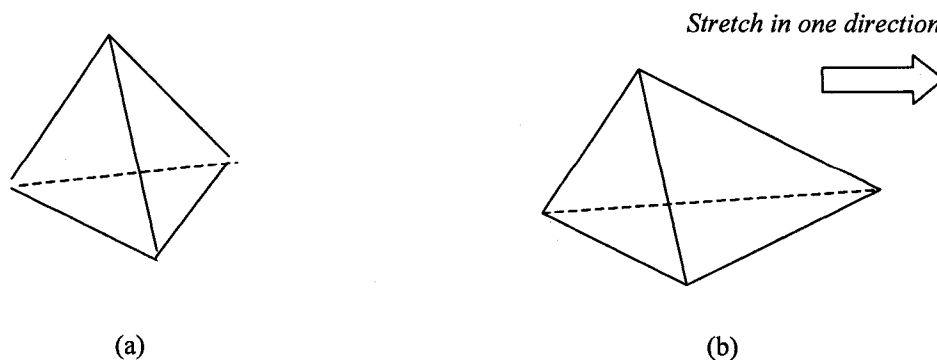
Figure 6.7: Second convergence test for the pedicle. An  $x$ -component shearing load was applied on one face while the opposite face was clamped. A mesh with at least 10000 elements is required for high accuracy in this case.

### 6.3.2 Reducing number of elements

As illustrated previously, the number of elements required for each substructure can be determined based on its convergence tests. In the examples presented in the previous section, where the desirable discrepancy is no more than 5%, the accuracy of the analysis can always be guaranteed but it comes at the expense of long computation times.

One way to reduce the computation time is to allow greater discrepancies when deciding on the number of elements based on the convergence curve. For our present purposes, discrepancies of up to 30% between the simulation results and the analytical results are considered to be “acceptable” based on the rationale that the uncertainties of the Young’s moduli of each substructure are much larger than 30%.

Another way of reducing the number of elements is to use longer and thinner tetrahedral elements as illustrated in Figure 6.8, in cases where the structure is much larger in one direction than in another. The quality of the mesh will, however, be affected, as the tetrahedral elements should ideally be equilateral for the best simulation results. A poorly meshed model is very likely to cause numerical errors during the solution process (e.g. Fried, 1972; Babuska and Aziz, 1976). Hence it is important not to over-stretch the elements. Technically, stretching the elements can be accomplished by applying a scaling factor to the mesh, in only one direction.



Reducing the number of elements can also be accomplished by changing the *unstructured size transition* in GiD, the mesh generation programme. The transition factor is a parameter that controls how rapidly elements are permitted to change in size from a high-resolution boundary to a low-resolution boundary.

Figure 6.9 shows two examples meshed with slow and fast transition, respectively. A slow transition results in many more elements, but mesh quality increases because a greater percentage of the elements are well shaped.

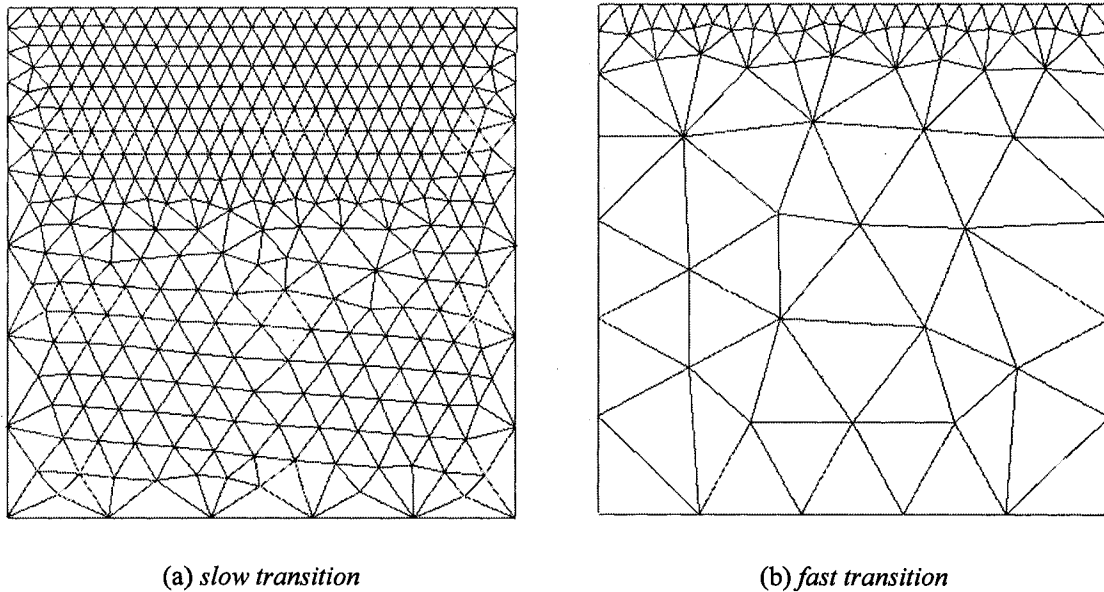


Figure 6.9: *Unstructured size transition parameter* determines the rate of change from a high-resolution boundary to a low-resolution boundary. In (a) and (b), the surface is meshed with a slow transition rate and a fast transition rate, respectively.

In GiD, the size transition is represented as a value from 0.0 (slow) to 1.0 (fast). For the pedicle-and-joint model, a size transition of 0.8 is used to reduce the number of elements. The scheme that involves stretching of the elements is not adopted because that could further reduce the quality of the final mesh.

In the final mesh, there are altogether 13209 tetrahedral elements in the model, and each simulation takes about one hour (PIII 700 MHz, 256 Mbytes RAM) to complete. It should be noted that the finite-element programme SAP IV fails under Windows on models with too many elements, as the intermediate file exceeds the 2 GBytes file size limit of Windows. The file size problem has been solved by running the programme under Linux.

## 6.4 Middle-ear model

### 6.4.1 Introduction

To obtain more convincing simulation results from the pedicle-and-joint model, realistic loading and boundary conditions are required. Obviously, having an applied load in only one or two directions is not good enough to simulate what really happens in the middle ear, as the 3-D vibrations of the eardrum, malleus and incus drive the pedicle. Similarly, having clamped the head of the stapes is a gross simplification of the true situation, in which the displacements of the stapes are constrained by the annular ligament, stapedial muscle and cochlear load. As a result, it is desirable to run tests on the pedicle-and-joint model within a middle-ear model.

Figure 6.10 shows a finite-element model of the cat middle ear which was developed in this laboratory (Funnell, 1996). The model includes shell representations of the eardrum and ossicles, and springs representing the middle-ear ligaments and cochlear load. The model of the eardrum is essentially the same as in previous models (Funnell, 1987, 1992). The footplate and the cochlear load are equivalent to the models described previously by Ladak and Funnell (1993, 1994). The incudostapedial joint is represented by a simple block formed by eight triangular shell elements (Ghosh and Funnell, 1995). Unlike its predecessors, this model does not have a fixed axis of rotation. Instead, the axis of rotation is determined by the ligaments, represented by springs, attached to the malleus and incus (Funnell, 1996).

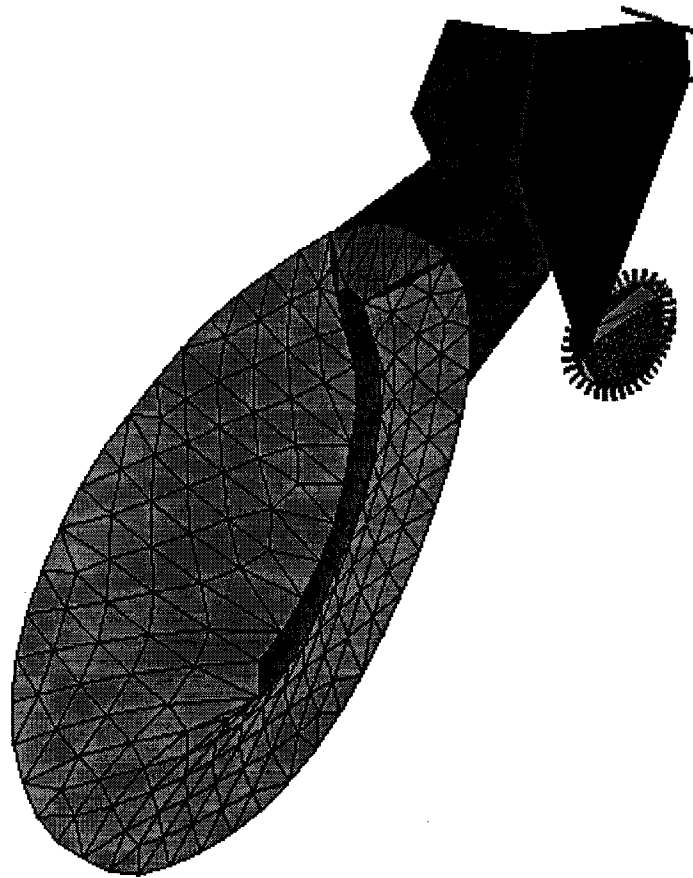


Figure 6.10: Previous finite-element model of cat middle ear

Details of the existing middle-ear model (Funnell, 1996) will be presented in the following three sections. The modifications made to it will be discussed in Section 6.4.5.

### *6.4.2 Eardrum*

As shown in Figure 6.8, the eardrum is represented by thin-shell elements. The conical shape of the eardrum is represented using circular arcs which have one end on the manubrium and the other along the tympanic ring. The degree of curvature of the arcs, expressed as a normalized radius of curvature, was set to 1.19 in this model (Funnell and Laszlo, 1977; Funnell, 1983).

The pars tensa is assigned a Young's modulus of 20 MPa, and a Poisson's ratio of 0.3. The overall thickness is estimated at 40  $\mu\text{m}$ , based on observations by Lim (1968).

### *6.4.3 Stapedial footplate*

The geometry and dimensions of the footplate were determined according to photomicrographs by Guinan and Peake (1967). The central portion and the rim of the footplate have thicknesses of 20  $\mu\text{m}$  and 200  $\mu\text{m}$ , respectively. Since the footplate is modelled as compact bone, it is given a Young's modulus of 20 GPa and a Poisson's ratio of 0.3.

Attaching the footplate to the oval window is the annular ligament. It constrains the displacements of the footplate and is represented by in-plane and out-of-plane springs evenly distributed along the circumference of the footplate (Ladak and Funnell, 1993). The model of the footplate is shown in Figure 6.11.

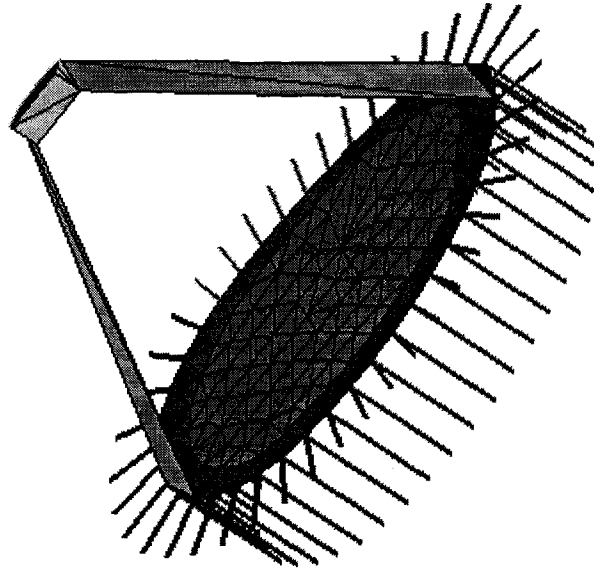


Figure 6.11: Finite-element model of stapes

The mechanical properties of each spring can be characterized by its stiffness (N/m). For the out-of-plane springs, which are perpendicular to the plane of the footplate, the total stiffness is

$$stiffness_{total} = \frac{area^2}{acoustic\ compliance} \quad (6.1)$$

where the acoustic compliance takes into account of the effects of both the annular ligament and the cochlear load. Given that the acoustic compliance is  $0.36 \times 10^{-14} \text{ m}^5/\text{N}$  (Lynch *et al.*, 1982) and the area of the footplate is  $1.26 \text{ mm}^2$  (Guninan and Peake, 1967), the total stiffness is calculated to be  $4.4 \times 10^2 \text{ N/m}$  (Ladak and Funnell, 1994). Thus, the stiffness of each spring is equal to the total stiffness divided by the number of springs. In this model, there are 40 out-of-plane springs and therefore each has a stiffness of 11 N/m.

The in-plane displacements of the footplate are constrained by the annular ligament which determines the stiffness of the in-plane springs. The dimensions of the annular ligament are considered to be uniform around its perimeter (Guinan and Peake, 1967).

The stiffness of a segment of the annular ligament, which is assumed to have a uniform rectangular cross section, is given by:

$$k = Et/l/w \quad (6.2)$$

where  $E$  is the Young's modulus,  $t$  is the thickness,  $l$  is the distance between adjacent nodes and  $w$  is the width. With the Young's modulus estimated at 10 kPa (Lynch et al., 1982) and the dimensions measured from a histological section (Guinan and Peake, 1967), Ladak and Funnell (1996) calculated the stiffness of each segment of annular ligament, and divided it equally between the springs at the two nodes. In this model, the in-plane springs are assigned a stiffness of 9.9 N/m.

#### 6.4.4 Supporting ligaments

The ligaments which support the ossicular chain are explicitly represented by springs. As shown in Figure 6.12, there are two sets of springs representing the ligaments which attach the middle-ear cavity to the anterior malleolar process and the posterior incudal process, respectively. To be consistent, the stiffness calculated previously by Funnell (1996) is adopted for the springs. It should be noted that these springs are highly simplified representations of the ligaments.

Following Funnell's approach (1996), the lateral bundle of the posterior incudal ligament is approximated by a cube with edges of 0.5 mm. Using the previously described equation  $k = Et/l/w$ , in which the Young's modulus  $E$  is taken to be 20 MPa, Funnell determined the total stiffness of the ligament to be 10 kN/m. For the medial bundle, which is about a third as thick, the stiffness is estimated to be 30 kN/m.

Similarly, three spring elements are used to model the elastic suspension of the malleus. In fact, it is a very crude representation because "the malleus appears to be attached to the

wall of the middle-ear cavity by a large but thin layer of amorphous material” (Funnell, 1996). For a surface area of  $2 \text{ mm}^2$ , and a thickness of  $0.1 \text{ mm}$ , the total stiffness is taken to be  $4 \text{ kN/m}$ .

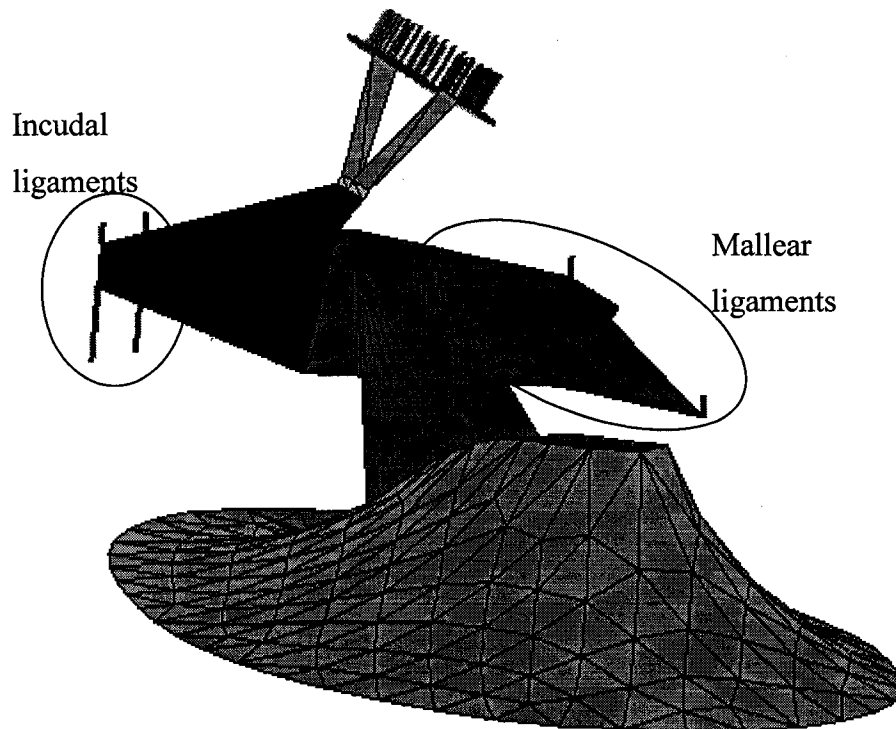


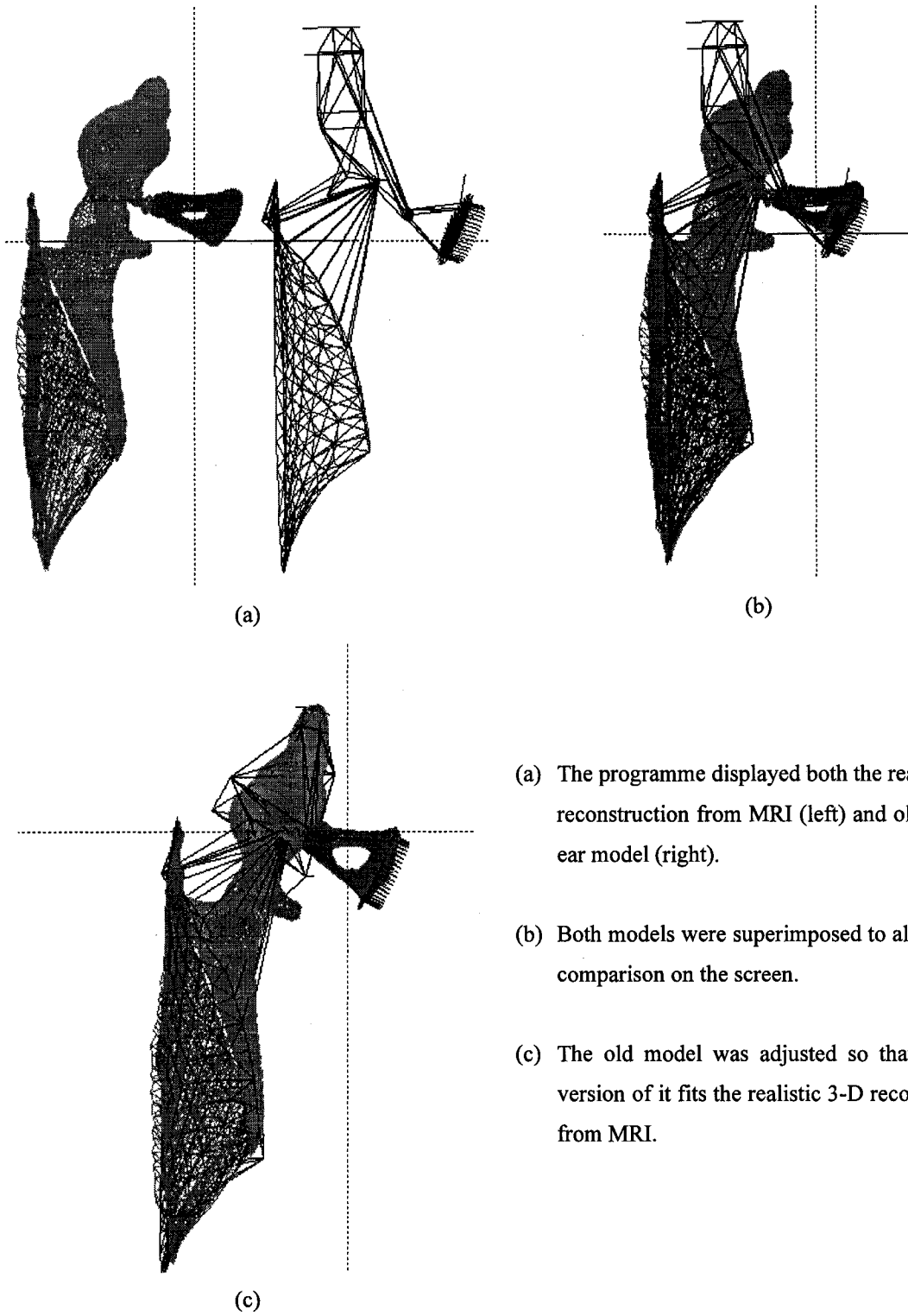
Figure 6.12: The malleus and incus are suspended by two sets of springs, representing mallear ligaments and incudal ligaments respectively.

### 6.4.5 Modifications

At the time the original middle-ear model was constructed, the high-resolution histology and MRI data were not yet available. Problems were found when comparing the original model with the most recent 3-D reconstructions from histology and MRI. Hence, some modifications were made to the original model, in particular to the alignment of the footplate and to the location of the elastic suspensions of the malleus and incus.

A new programme was developed to offer a friendly environment to display and manipulate the finite-element models. The programme was implemented with OpenGL in C. As illustrated in Figure 6.13, the basic principle of the programme is to allow the user to superimpose two models and adjust the old model to fit the realistic 3-D reconstructions from histology or MRI.

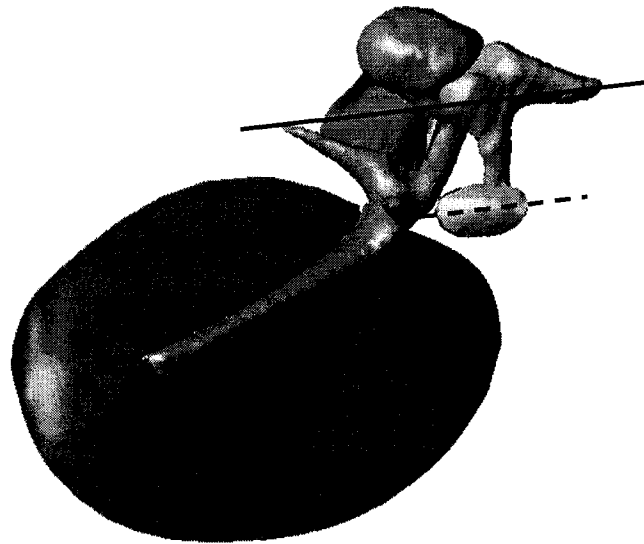
The programme displays the 3-D reconstruction and the finite-element model simultaneously, allowing direct comparison by inspection on the screen. Using the eardrum as reference, two models are superimposed as the first step. The user then selects parts, i.e. the stapes, which require changes. The user can translate and rotate the selected parts of the old model in the  $x$ ,  $y$  and  $z$  directions. The programme also provides features such as zoom, change of viewing angles, change of the degree of rotation, etc.



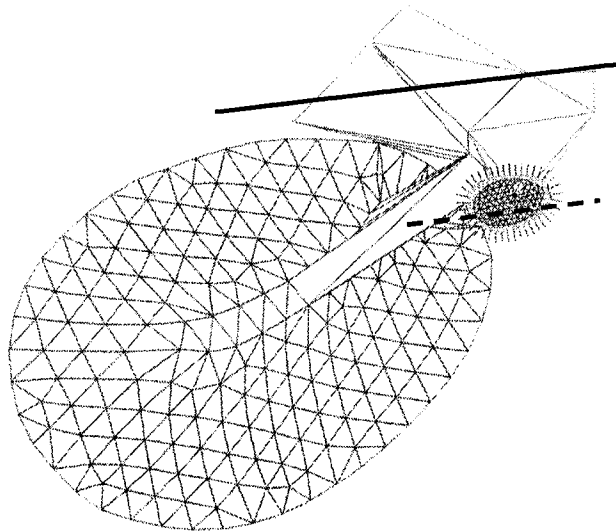
- (a) The programme displayed both the realistic 3-D reconstruction from MRI (left) and old middle-ear model (right).
- (b) Both models were superimposed to allow direct comparison on the screen.
- (c) The old model was adjusted so that the new version of it fits the realistic 3-D reconstruction from MRI.

Figure 6.13: Screen shots of the programme.

Figure 6.14(a) and (b) show the 3-D reconstruction from MRI and the modified finite-element model of the middle ear, respectively. The bold line shown in the figure is the supposed axis of rotation, corresponding to the classical concept of a fixed axis through the anterior process of the malleus and the posterior process of the incus. The fixed axis of rotation is roughly parallel to the long axis of the footplate. Illustrations of the models from different perspectives are shown in Figure 6.15.

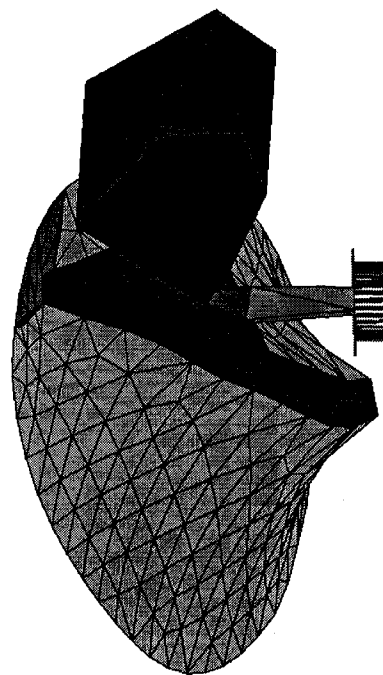


(a)

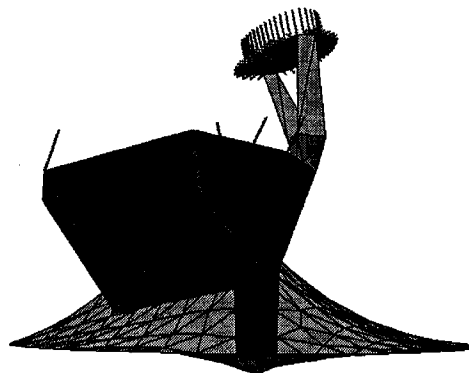
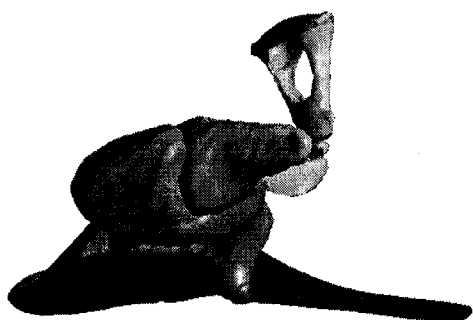


(b)

Figure 6.14: (a) 3-D reconstruction from MRI. (b) Finite-element model of middle ear. The solid bold lines correspond to the classical axis of rotation, running from the anterior malleolar tip to the posterior incudal tip. The dashed lines correspond to the long axis of the footplate.



(a)



(b)

Figure 6.15: 3-D reconstruction from MRI and finite-element model of middle ear viewed from different perspectives.

The pedicle-and-joint model has been incorporated into the middle-ear model (Figure 6.16). Careful attention has been paid to the pedicle-and-joint model's alignment, which is determined based on the 3-D reconstruction from the histological data of the middle ear. The complete model of the middle ear is shown in Figure 6.17.

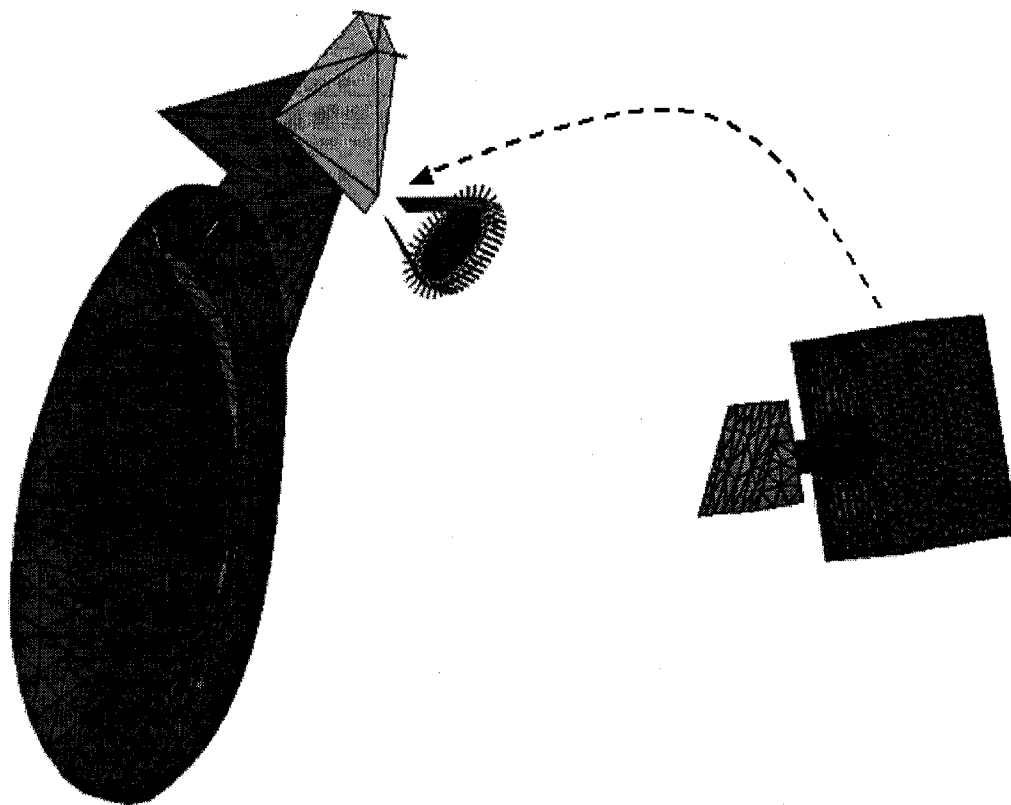
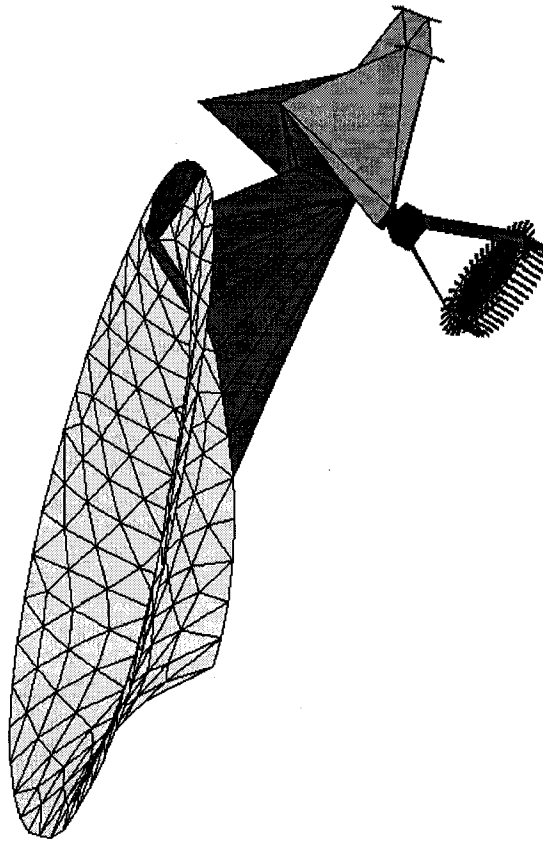
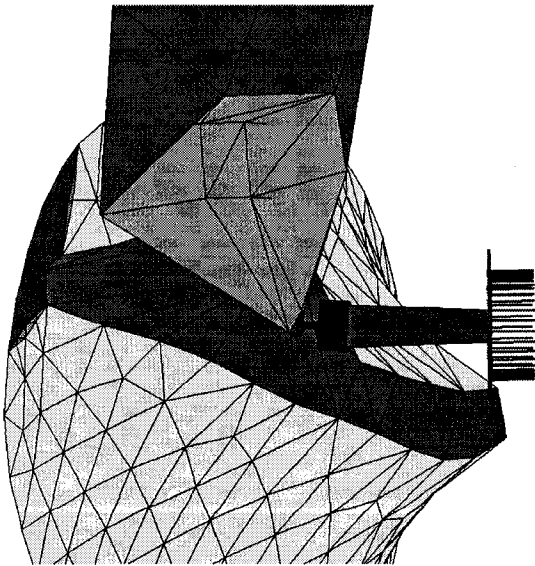


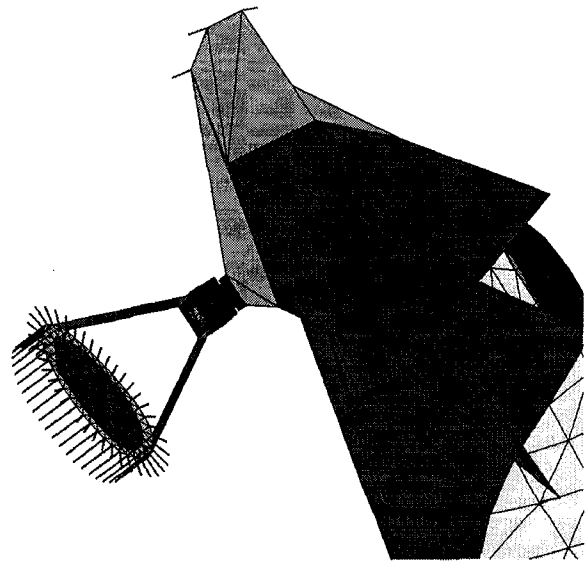
Figure 6.16: The pedicle-and-joint model is incorporated in the middle-ear model, replacing the old representation of the incudostapedial joint.



(a)



(b)



(c)

Figure 6.17: (a) Finite-element model of middle ear after including the pedicle-and-joint model.  
(b)(c) Pedicle-and-joint model within the middle-ear model from different perspectives.

## 6.5 Bandwidth minimization

The computation time can be greatly reduced if the nodes of the mesh are numbered in a specific order that minimizes the bandwidth, the width of the band of non-zero numbers which lies along the diagonal of the stiffness matrix. For the models presented here, the minimization of the bandwidth is performed, using a bandwidth-minimization programme written by Funnell, based on the algorithm of Crane *et al* (1976).

## 6.6 Input stimulus

For the isolated pedicle-and-joint model, the exact input is not known but it can be simulated with small loads for the purposes of this study. A uniform static pressure was applied on the long process of the incus; one surface of the head of the stapes was clamped (Figure 6.18). The simulation results for this model will be discussed in Section 7.1.

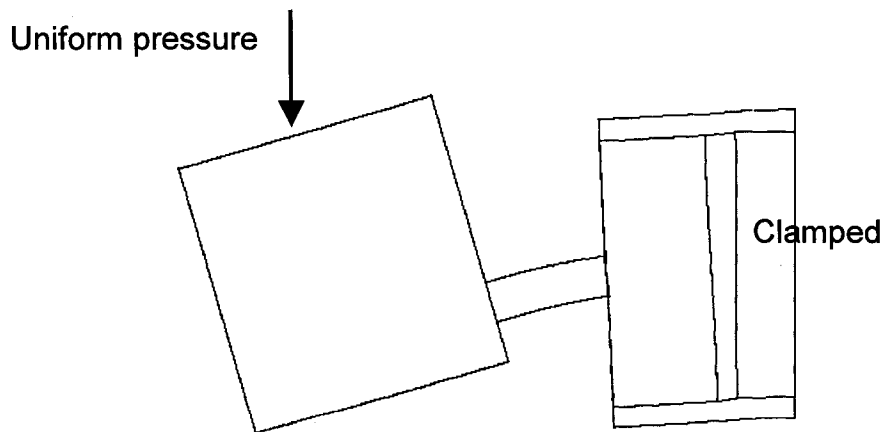


Figure 6.18: A uniform pressure was applied the pedicle-and-joint model. One surface of the head of the stapes was clamped.

For the middle-ear model, a uniform sound pressure of 100 dB SPL, equivalent to 2.828 Pa, is applied to the eardrum. Since the middle ear behaves linearly up to 130 dB SPL (Guinan and Peake, 1967), the assumption of linearity in this model is not violated. The frequency of the input is taken to be low enough so that the damping and inertial effects can be ignored.

## Chapter 7

### RESULTS

#### 7.1 Pedicle-and-joint model

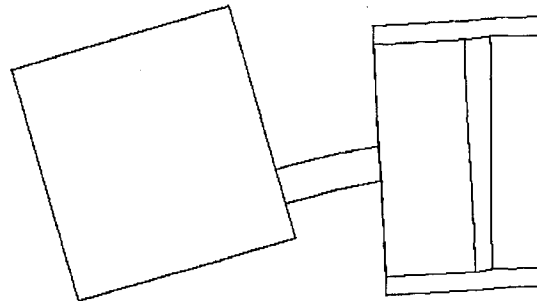
##### *7.1.1 Introduction*

Section 7.1 presents the simulation results of the isolated pedicle-and-joint model. As discussed in the preceding sections, the mechanical properties of the middle-ear structures are uncertain and therefore the tests are designed explore variations in the Young's moduli of various substructures in the pedicle-and-joint model. Section 7.1.2 shows the results for the base case in which a set of plausible estimates of the Young's moduli, as discussed in Chapter 6, is adopted. The results after varying the Young's moduli of the pedicle and the joint are presented in Section 7.1.3 and 7.1.4, respectively. A summary of the results of the isolated pedicle-and-joint model is presented in Section 7.1.5.

As the displacements of the ossicles are on the order of nm ( $10^{-9}$  m), the simulated deformations presented here were scaled up so that the displacements can be seen.

### 7.1.2 Base case

Figure 7.1 shows the simulation results for the isolated pedicle-and-joint model in which the Young's moduli of its substructures are as given (refer to Sections 6.2.2 to 6.2.6) in Table 7.1.



*Pedicle: 5 GPa; joint gap: 10 MPa; capsule: 50 MPa*

Figure 7.1: The simulation results for the base case. The deformations were scaled up so that the displacements, on the order of nm, can be seen.

	<b>Young's modulus (Pa)</b>
<b>Long process of incus</b>	12 G
<b>Pedicle</b>	5 G
<b>Lenticular plate</b>	1 G
<b>Joint gap</b>	10 M
<b>Head of stapes</b>	1 G
<b>Joint capsule</b>	50 M

Table 7.1: The Young's moduli of the substructures in the pedicle-and-joint model in the base case.

One way to evaluate the results shown in Figure 7.1 is to examine the contributions of the pedicle and the joint to the overall flexibility. If there is a significant bending of the pedicle while the incudostapedial joint appears to be relatively rigid, it suggests that the presence of the pedicle has an effect on the mechanics of the ossicles.

Figure 7.1 shows that the load transmission from the incus to the stapes is affected by both the pedicle and the incudostapedial joint. There is a comparatively large bending at the pedicle even though it is made of bone.

The statements above are made by inspection and it is difficult to interpret the figure quantitatively. To allow quantitative comparison, angles  $\alpha$  and  $\beta$ , defined in Figure 7.2, were measured in each case of the simulation results. The value of  $\alpha + \beta$  corresponds to the overall flexibility of the pedicle-and-joint model. The ratio  $\beta/\alpha$  provides a measure of the relative contributions of the pedicle and incudostapedial joint to the overall flexibility. The greater the value, the more significant was the contribution of the pedicle to the overall flexibility.

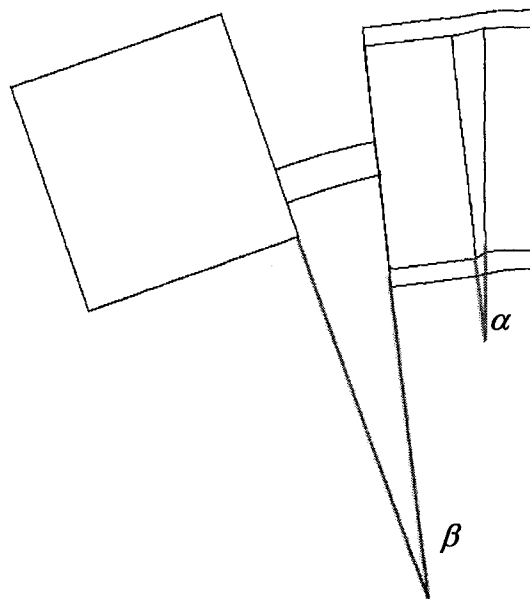


Figure 7.2: An example of the simulation results in which the displacements were scaled up for the purposes of illustration. Angles  $\alpha$  and  $\beta$  as defined in the figure provide a method for quantitative comparison among the results.

There are different methods for calculating the angles  $\alpha$  and  $\beta$ , and the following example demonstrates the method used in this thesis.

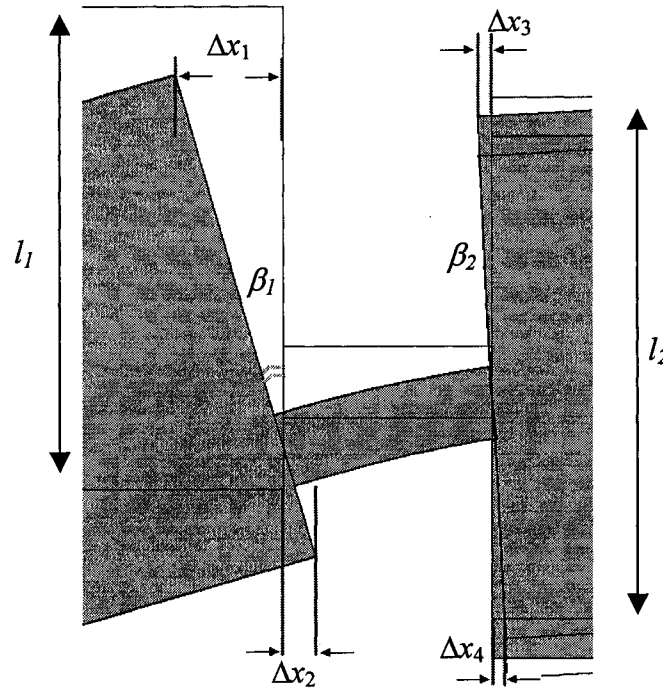


Figure 7.3: An illustration showing how the angle  $\beta$  is calculated.

As illustrated in Figure 7.3, the angle  $\beta$  is given by

$$\begin{aligned} \beta &= \beta_1 - \beta_2 \\ &= \sin^{-1} \frac{\Delta x_1 - \Delta x_2}{l_1} - \sin^{-1} \frac{\Delta x_3 - \Delta x_4}{l_2} \end{aligned} \quad (7.1)$$

Since the angles  $\beta_1$  and  $\beta_2$  are very small, equation 7.1 can be rewritten as

$$\beta \cong \frac{\Delta x_1 - \Delta x_2}{l_1} - \frac{\Delta x_3 - \Delta x_4}{l_2} \quad (7.2)$$

For the base case, the values of the angles  $\alpha$ ,  $\beta$ ,  $\alpha+\beta$  and the ratio  $\beta/\alpha$  are listed in Table 7.2. In this case, the bending at the pedicle is significant since the angle  $\beta$  is about seven times greater than  $\alpha$ .

	$\alpha$ ( $\mu\text{rad}$ )	$\beta$ ( $\mu\text{rad}$ )	$\alpha+\beta$ ( $\mu\text{rad}$ )	$\beta/\alpha$
p:5 G; j:10 M; c:50 M (Base case)	1.663	11.77	13.433	7.075

Table 7.2: Angles  $\alpha$ ,  $\beta$ ,  $\alpha+\beta$  and the ratio  $\beta/\alpha$  for the base case. The Young's moduli (measured in Pa) of the pedicle, joint gap and capsule are represented by  $p$ ,  $j$  and  $c$ , respectively.

### 7.1.3 Variation of joint stiffness

The Young's moduli of the joint gap and capsule were varied as discussed in Chapter 6. The simulation results are shown in Figure 7.4. The values of the angles  $\alpha$ ,  $\beta$ ,  $\alpha+\beta$  and the ratio  $\beta/\alpha$  for these cases listed in Table 7.3. For these cases, the pedicle bending ( $\beta$ ) is almost constant at 11.8.

In Figure 7.4 (a), the flexibility of the joint increases since the Young's modulus of the joint gap is reduced from 10 MPa to 5 MPa. The value of  $\alpha$  increases by 40% as the stiffness of the joint gap decreases by 50%.

In Figure 7.4 (b) and (c), the Young's modulus of the joint capsule was reduced from 50 MPa to 20 MPa, and increased to 100 MPa, respectively. For case (b), the 60% decrease of the capsule stiffness leads to a 66% increase of angle  $\alpha$ . For case (c), the doubling of the capsule stiffness results in a 42% decrease of the angle  $\alpha$ .

In Figure 7.4 (d), the Young's moduli of the joint gap and the capsule were both reduced, to values of 5 MPa and 20 MPa, respectively. The value of  $\alpha$  increases by 170%. The

flexibility of the joint increases most in this case. The pedicle bending is less significant compared with those in cases (a) (b) (c), but  $\beta$  is still more than twice as large as  $\alpha$

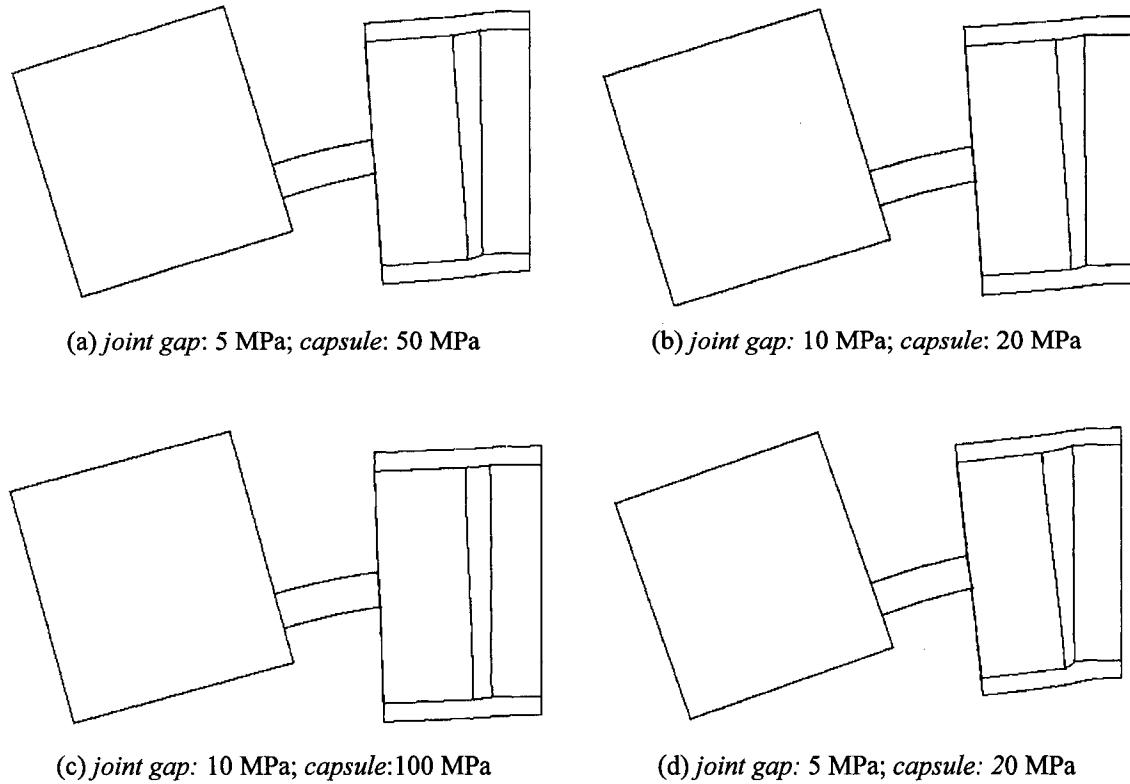


Figure 7.4: The simulation results for cases in which the Young's moduli of the capsule and joint gap vary. The Young's modulus of the pedicle is fixed at 5 GPa. The deformations were scaled up so that the displacements, on the order of nm, can be seen.

	$\alpha$ ( $\mu\text{rad}$ )	$\beta$ ( $\mu\text{rad}$ )	$\alpha+\beta$ ( $\mu\text{rad}$ )	$\beta/\alpha$
(a) p:5 G; j:5 M; c:50 M	2.348	11.83	14.178	5.039
(b) p:5 G; j:10 M; c:20 M	2.760	11.71	14.47	4.243
(c) p:5 G; j:10 M; c:100 M	0.959	11.81	12.77	12.317
(d) p:5 G; j:5 M; c:20 M	4.482	11.77	16.252	2.625

Table 7.3: Angles  $\alpha$ ,  $\beta$ ,  $\alpha+\beta$  and the ratio  $\beta/\alpha$  for cases in which the Young's moduli of the capsule and joint gap vary. The Young's moduli (measured in Pa) of the pedicle, joint gap and capsule are represented by  $p$ ,  $j$  and  $c$ , respectively.

#### 7.1.4 Variation of pedicle stiffness

Figure 7.5 shows the simulation results where the Young's modulus of pedicle varies as discussed in Chapter 6. The values of the angles  $\alpha$ ,  $\beta$ ,  $\alpha+\beta$  and the ratio  $\beta/\alpha$  for these cases are listed in Table 7.4.

In Figure 7.5 (a) the pedicle stiffness was increased from 5 GPa to 12 GPa, to equal that of the long process of the incus. As the pedicle becomes stiffer, the degree of the pedicle bending decreases by 35% but it is still about 4.5 times as large as that of the joint.

In Figure 7.5 (b) the Young's modulus of the pedicle was reduced from 5 GPa to 3 GPa. In contrast to case (a), the degree of the pedicle bending increases by 39% and this case results in a significant increase of the ratio  $\beta/\alpha$ . It also has the highest value of  $\alpha+\beta$ , indicating the greatest flexibility of the pedicle-and-joint model.

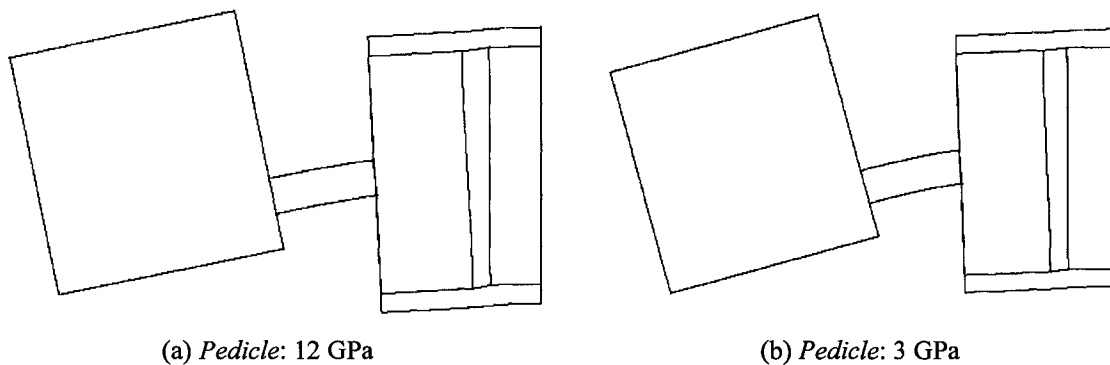


Figure 7.5: The simulation results for cases in which the Young's modulus of the pedicle varies. The deformations were scaled up so that the displacements, on the order of nm, can be seen. The Young's moduli of the joint gap and capsule are fixed at value of 10 MPa and 50 MPa, respectively.

	$\alpha$ ( $\mu\text{rad}$ )	$\beta$ ( $\mu\text{rad}$ )	$\alpha+\beta$ ( $\mu\text{rad}$ )	$\beta/\alpha$
(a) $p=12$ G; $j=10$ M; $c=50$ M	1.663	7.596	9.259	4.569
(b) $p=3$ G; $j=10$ M; $c=50$ M	1.664	16.40	18.064	9.860

Table 7.4: Angles  $\alpha$ ,  $\beta$ ,  $\alpha+\beta$  and the ratio  $\beta/\alpha$  for cases in which the Young's modulus of the pedicle varies. The Young's moduli (measured in Pa) of the pedicle, joint gap and capsule are represented by  $p$ ,  $j$  and  $c$ , respectively.

### 7.1.5 Summary

In general, the bending at the pedicle is more significant than the flexing at the incudostapedial joint since the ratios  $\beta/\alpha$  are always greater than 2.5 for these parameters. Relative contributions to the overall bending vary as expected as the parameters are varied.

The change of the moduli of the joint and capsule has little effect on the bending at the pedicle. Conversely, the change of the modulus of the pedicle has little effect on the bending of the joint and capsule. The flexibility of the joint increases most when the Young's moduli of the joint and the capsule are both reduced; their respective contributions to the increased flexibility are roughly the same. The pedicle bends most when its stiffness is reduced: decreasing its Young's modulus by 40% increases  $\beta$  by about the same percentage.

## **7.2 Middle-ear model**

### *7.2.1 Introduction*

As stated in Section 6.4, the loading and boundary conditions in the isolated pedicle-and-joint model are highly simplified. As a result, the pedicle-and-joint model has been included in the middle-ear model for more sophisticated investigation (Figure 6.16).

The middle-ear model is suspended by springs representing the suspending ligaments and cochlear loads. A uniform sound pressure of 100 dB SPL is applied to the eardrum. Once again, a range of plausible values is used for the Young's moduli for the pedicle, joint and capsule.

### *7.2.2 Validation of the middle-ear model*

#### **7.2.2.1 Static displacements of the eardrum**

Figure 7.6 shows the low-frequency vibration pattern of the eardrum in the middle-ear model. The maximum eardrum displacement and the umbo displacement can be used to characterize the eardrum and manubrium movements. For the middle-ear model presented here, the maximum eardrum displacement (308 nm) is about 2.3 times as large as the umbo displacement (135 nm). The vibration pattern and the magnitudes of the maximum displacements are similar even when the stiffness of the pedicle-and-joint part of the model changes. The results are similar to the results obtained in earlier models developed by Ghosh (1996) and Funnell (1996). For those two earlier models, the maximum eardrum displacement and the umbo displacement are 232 nm and 74 nm, and 258 nm and 105 nm, respectively.

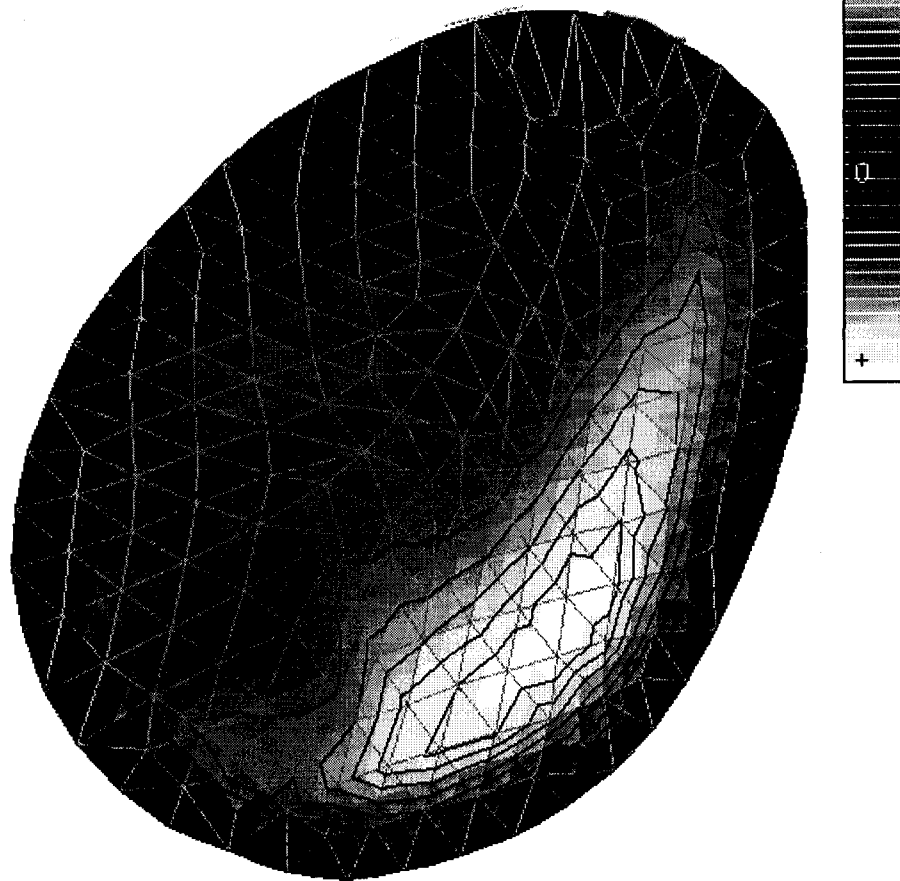


Figure 7.6: Vibration pattern of the eardrum. The maximal displacements of the eardrum and manubrium are 308 and 135, respectively.

### 7.2.2.2 Footplate displacements

The displacement of the central node is used here to represent the displacement of the footplate. For the middle-ear model presented here, the footplate displacements in the  $x$ ,  $y$  and  $z$  directions are 3.71 nm/Pa, 4.17 nm/Pa and 11.3 nm/Pa, respectively. The footplate displacement in the  $z$  direction is, as expected, greater than that in the other directions. The magnitude of the  $z$  displacement is, however, only about one third of the values of the experimental measurement (Guinan and Peake, 1967; Decraemer *et al.*, 2000). Table 7.5 lists the values of the maximum eardrum displacement, umbo displacement (maximum manubrium displacement), and footplate displacement in the  $z$  direction, as reported by different authors.

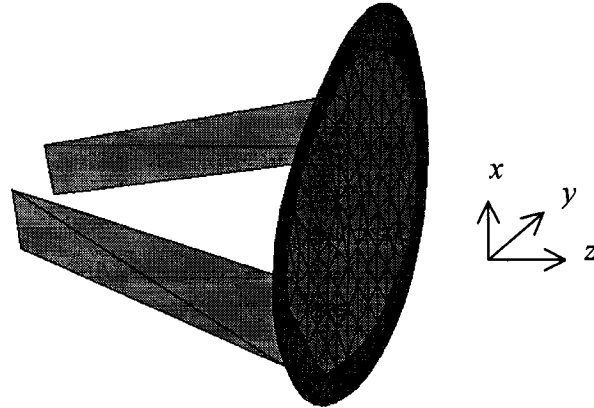


Figure 7.7: Finite-element model of the footplate.

	Maximum displacement of the eardrum	Displacement of the umbo	z displacement of the footplate
Ghosh (1996) *	232 nm	74 nm	29 – 36 nm
Funnell (1996)	258 nm	105 nm	5.5- 7.5 nm
Model presented here	308 nm	135 nm	11.3 nm
<b>Experimental measurement</b>			
Guinan & Peake (1967)	-	53 nm	25 – 30 nm
Decraemer <i>et al.</i> (2000)	-	-	30 nm

Table 7.5: The values of the maximum eardrum displacement, umbo displacement, and footplate displacement in the z direction, reported by different authors. The frequency of the input stimulus is below 100 Hz. The displacements are normalized to a stimulus of 1 Pa.

\* Finite-element model has a fixed rotation axis

The finite-element models of middle ear listed in Table 7.5 include the middle-ear model presented in this thesis, and the models developed by Ghosh (1996) and Funnell (1996). The middle-ear model constructed by Ghosh (1996) is the earliest among the three, and it has a fixed rotation axis. An improved version of that model was constructed by Funnell in 1996. For the improved model, the rotation axis is determined by the suspending ligaments, and the representations of the ossicles are greatly improved. For the middle-ear model presented here, the alignment problem in its predecessors has been corrected. In addition, a pedicle-and-joint representation is included in the model.

Although the three middle-ear models are closely related, there are clear differences, especially in the representation of the ossicles. That may explain the differences in the maximum eardrum displacement and the umbo displacement among the three models, as shown in Table 7.5. For the three middle-ear models, the ratio between the maximum eardrum displacement and the umbo displacement is nevertheless roughly the same.

In the model constructed by Ghosh (1996), the distance between the stapes and the plane of the tympanic ring is about three times greater than that in the anatomy, and that results in a much greater lever ratio of the ossicles. That explains the large  $z$  component of the footplate displacement which is about three times greater than that of the other two models listed in Table 7.5.

The discrepancy of the  $z$  component of the footplate displacement between the simulation results and the experimental measurements could come from many sources in the middle-ear model: uncertainties of the Young's moduli, highly simplified representation of the supporting ligaments, insufficiency of finite elements in the mesh, etc.

To examine the effect of the supporting-ligament alignment on the  $z$  component of the footplate displacement, 15 test cases were designed having different alignments for the springs representing the ligaments. In one trial, the  $z$  displacement of the footplate could be increased by ~20%. A simulation was also done with a fixed axis of rotation, in case the flexibility of the supporting springs was responsible for the decreased footplate displacement, but this did not seem to be the case. The hours of simulation time discourage any further effort to tune up the displacement just by trial and error.

### 7.2.2.3 Axis of rotation

Figure 7.8 shows the medial view of the displacement-amplitude contours of the model. The contour with zero displacement indicates the position of the axis of rotation. As expected, the axis of rotation is roughly parallel to the classical fixed axis, running from the anterior malleolar tip to the posterior incudal tip.

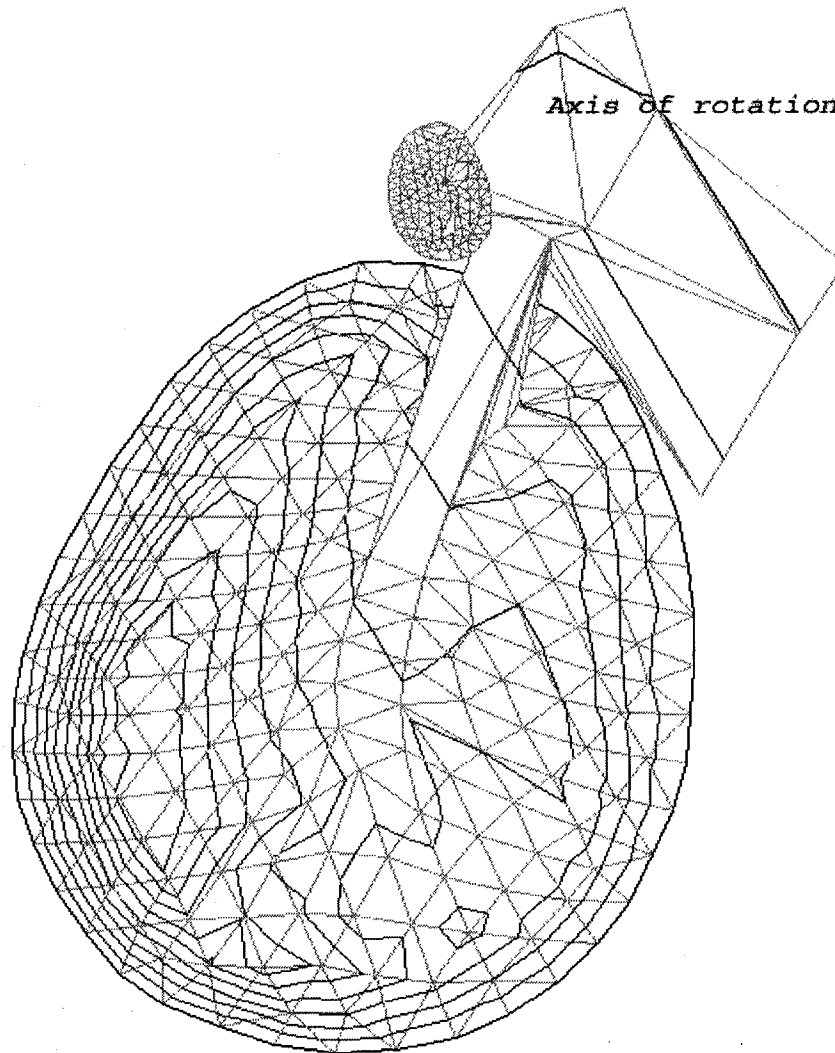
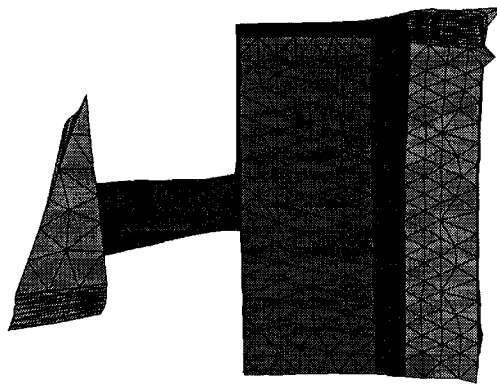


Figure 7.8: Visualisation of the displacement pattern for the displacement component along the axis normal to the plane of the page. The axis of rotation for this model is roughly parallel to the classical axis of rotation.

### 7.2.3 Pedicle-and-joint model

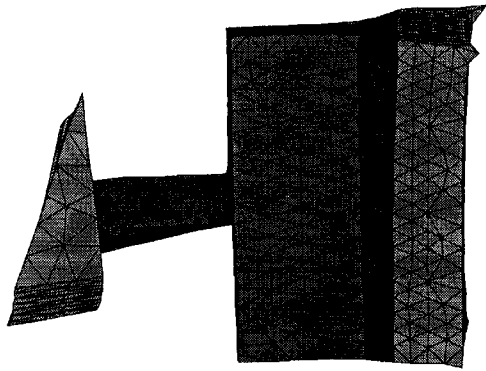
The simulation results for the pedicle-and-joint part of the middle-ear model will be evaluated in the same manner as described in Section 7.1. Figure 7.9 shows the results for the base case; Figure 7.10 and 7.11 show the results after varying the stiffness of the joint and pedicle, respectively. The deformations are scaled up so that the displacements, on the order of nm, can be seen.

Table 7.6 lists the measurements of  $\alpha$ ,  $\beta$ ,  $\alpha+\beta$  and the ratio  $\beta/\alpha$  in these seven different cases.

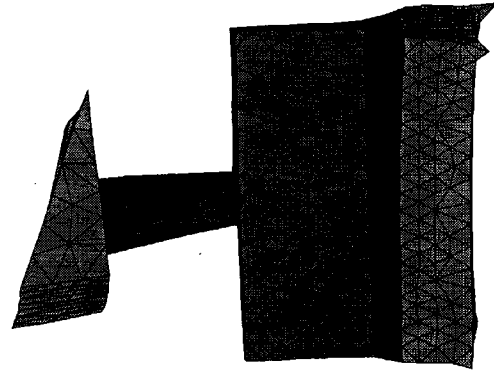


*Pedicle: 5 GPa; joint gap: 10 MPa; capsule: 50 MPa*

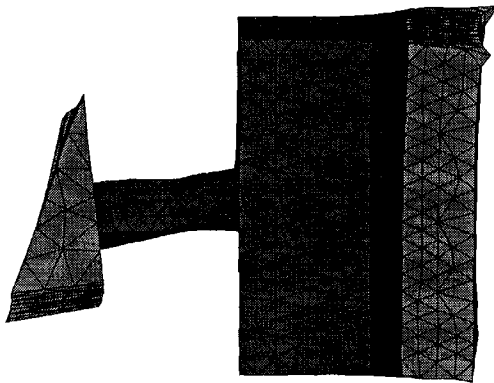
Figure 7.9: The simulation results for the pedicle-and-joint part in the middle-ear model for the base case.



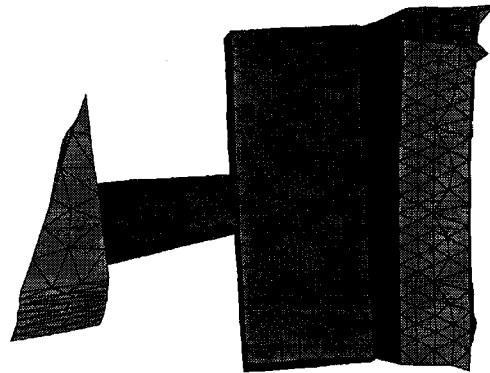
(a) *joint gap: 5 MPa; capsule: 50 MPa*



(b) *joint gap: 10 MPa; capsule: 20 MPa*



(c) *joint gap: 10 MPa; capsule: 100 MPa*



(d) *joint gap: 5 MPa; capsule: 20 MPa*

Figure 7.10: The simulation results for the pedicle-and-joint part in the middle-ear model, for cases in which the Young's moduli of the capsule and joint gap vary. The Young's modulus of the pedicle is fixed at 5 GPa.

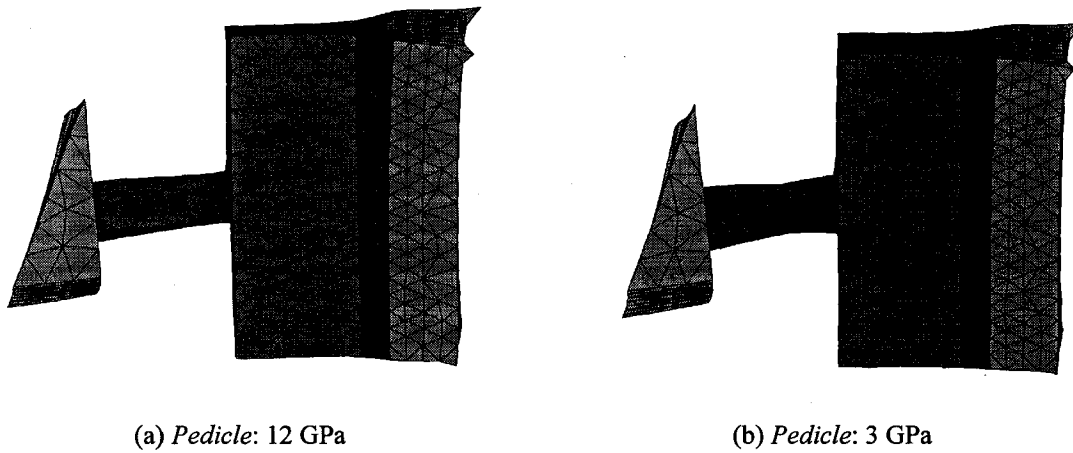


Figure 7.11: The simulation results for the pedicle-and-joint part in the middle-ear model, for cases in which the Young's modulus of the pedicle varies. The Young's moduli of the joint gap and capsule are fixed at value of 10 MPa and 50 MPa, respectively.

<b>Pedicle-and-joint part in middle-ear model</b>				
	$\alpha$	$\beta$	$\alpha+\beta$	$\beta/\alpha$
	( $\mu\text{rad}$ )	( $\mu\text{rad}$ )	( $\mu\text{rad}$ )	
(a) $p=5\text{ G}; j=10\text{ M}; c=50\text{ M}$ <i>Base Case</i>	1.405	9.595	11.000	6.827
(b) $p=5\text{ G}; j=5\text{ M}; c=50\text{ M}$	1.838	9.290	11.128	5.045
(c) $p=5\text{ G}; j=10\text{ M}; c=20\text{ M}$	2.027	9.401	11.428	4.638
(d) $p=5\text{ G}; j=10\text{ M}; c=100\text{ M}$	0.972	9.966	10.938	10.243
(e) $p=5\text{ G}; j=5\text{ M}; c=20\text{ M}$	3.020	8.811	12.019	2.911
(f) $p=12\text{ G}; j=10\text{ M}; c=50\text{ M}$	1.514	7.697	9.211	5.086
(g) $p=3\text{ G}; j=10\text{ M}; c=50\text{ M}$	1.324	11.132	12.456	8.405

Table 7.6: Angles  $\alpha$ ,  $\beta$ ,  $\alpha+\beta$  and the ratio  $\beta/\alpha$  for the seven different cases shown in Figure 7.9, 7.10 and 7.11. The Young's moduli (measured in Pa) of the pedicle, joint gap and capsule are represented by  $p$ ,  $j$  and  $c$ , respectively.

The simulation results are consistent with those obtained when the pedicle-and-joint model was tested alone. The results suggest that most of the flexibility between the incus and the stapes actually originates from the pedicle rather than from the incudostapedial joint.

Table 7.7 summarizes the measurements of  $\alpha$ ,  $\beta$ ,  $\alpha+\beta$  and the ratio  $\beta/\alpha$  for the isolated pedicle-and-joint model. Tables 7.6 and 7.7 both indicate that reducing the stiffness of the pedicle results in the greatest values of  $\beta$ ,  $\alpha+\beta$  and  $\beta/\alpha$ . The value of  $\alpha$ , a measure of the joint flexibility, increases most when the Young's moduli of the joint and the capsule are both reduced. In contrast, the flexibility of the joint decreases drastically when the Young's modulus of the joint capsule is increased to 100 MPa.

There is a twisting at the pedicle-and-joint model within the middle-ear model. The presence of the twisting is not very surprising since the motion of the ossicles is complicated. Indeed, the twisting may correspond to the in-plane rotation of the footplate as discussed in Chapter 3.

<b>Isolated pedicle-and-joint model</b>				
	$\alpha$ ( $\mu\text{rad}$ )	$\beta$ ( $\mu\text{rad}$ )	$\alpha+\beta$ ( $\mu\text{rad}$ )	$\beta/\alpha$
(b) $p=5$ G; $j=10$ M; $c=50$ M <i>Base Case</i>	1.663	11.77	13.433	7.075
(b) $p=5$ G; $j=5$ M; $c=50$ M	2.348	11.83	14.178	5.039
(c) $p=5$ G; $j=10$ M; $c=20$ M	2.760	11.71	14.47	4.243
(d) $p=5$ G; $j=10$ M; $c=100$ M	0.959	11.81	12.77	12.317
(e) $p=5$ G; $j=5$ M; $c=20$ M	4.482	11.77	16.252	2.625
(f) $p=12$ G; $j=10$ M; $c=50$ M	1.663	7.596	9.259	4.569
(g) $p=3$ G; $j=10$ M; $c=50$ M	1.664	16.40	18.064	9.860

Table 7.7: Angles  $\alpha$ ,  $\beta$ ,  $\alpha+\beta$  and the ratio  $\beta/\alpha$  for the isolated pedicle-and-joint model. The Young's moduli (measured in Pa) of the pedicle, joint and capsule are represented by  $p$ ,  $j$  and  $c$ , respectively.

In the results shown in Figures 7.9 to 7.11, there are “ears” at the corners of the stapes head. It should be noted that for simplicity the crura have been attached only to the four corners (nodes) of the stapes head of the pedicle-and-joint model. The stresses from the stapes head are transferred to the crura only via four nodes, and therefore these four nodes have greater displacements compared with other nodes on the stapes-head surface.

These “ears” indicate that part of the energy transferred from the stapes head to the crura has been dissipated, and that could affect the accuracy of the simulation results. One way to solve the problem is to use more nodes to attach the stapes head to the crura.

Figure 7.12 shows a close-up view of the “ears”.

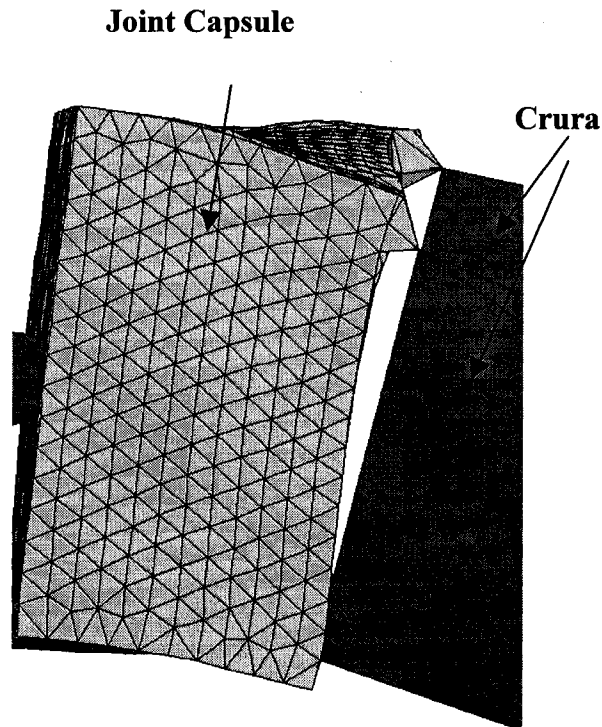


Figure 7.12: Close-up view of the “ears”.

## Chapter 8

# CONCLUSION AND FUTURE WORK

### 8.1 Conclusion

This is the first attempt to model the pedicle and the incudostapedial joint in such detail. A great deal of effort was devoted to the mesh generation and material properties of the model. The pedicle-and-joint model was tested in two different ways. On the one hand, the model was tested in isolation; on the other hand, the model was tested within an existing middle-ear model. The model was subjected to a low-frequency load, where the effects of inertia and damping are negligible.

The pedicle-and-joint model consists of the end of the long process of the incus, the pedicle, the lenticular plate, the joint gap, the joint capsule, and the head of the stapes. The shape and dimensions of the model were based on histological sections of a cat middle ear. Special attention has been paid to the material properties of the structures in the models. Possible values for the Young's moduli of the joint, joint capsule and pedicle were examined.

The pedicle-and-joint model was constructed using tetrahedral elements. Convergence tests were conducted to determine the number of elements required for each substructure in the model. The issue of the compromise between the mesh resolution and the computation time was investigated.

An existing finite-element model of the cat middle ear was modified to include the new pedicle-and-joint component. Some alignment problems of the old model were found when comparing it with the most recent 3-D reconstructions from histology and MRI. To solve the problems, a programme was developed to offer a friendly environment to display and manipulate the finite-element models.

The simulation results of the middle-ear model are consistent with those of the simple pedicle-and-joint model. The results suggest that the bending at the pedicle is more significant than the flexing at the incudostapedial joint. In other words, most of the flexibility between the incus and the stapes actually originates from the bony pedicle rather than from the incudostapedial joint itself.

## 8.2 Future Work

The next phase of the project will be to use more realistic models which are constructed based on histology and/or MRI. For example, the modelling of the form of the pedicle should be improved. In fact, as shown in Figure 8.1, more realistic surface models of the pedicle and the middle ear have recently been developed in the laboratory. In addition, the estimates of the parameters used in the model, such as the Young's moduli, should ideally be refined using data derived from experimental studies on the middle ear itself rather than the existing measurements on other parts of the body.

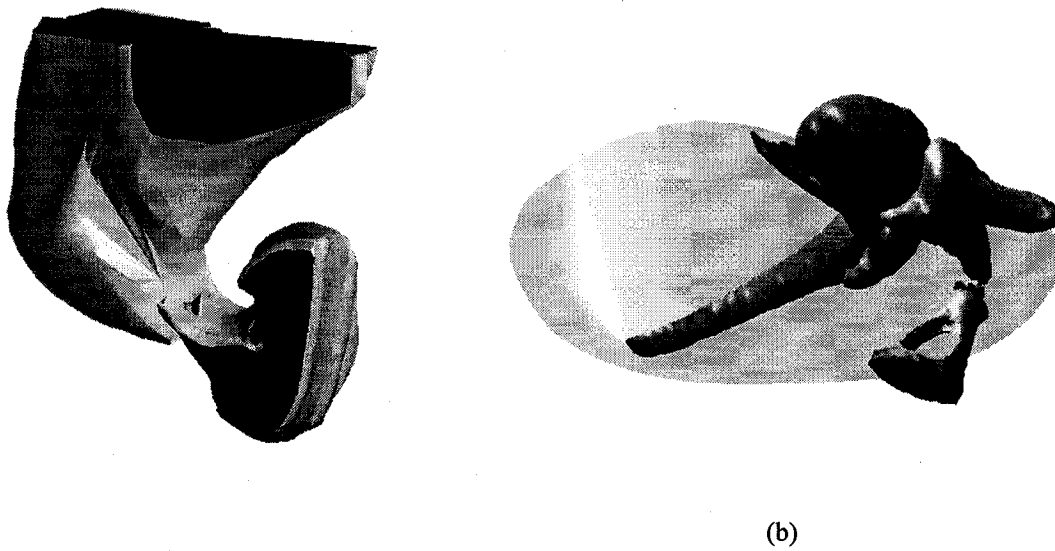


Figure 8.1: More realistic models of (a) lenticular process and (b) cat middle ear. Both models were constructed by Funnell.

Long computation time is one of the main problems for the model presented here, and will get even more serious for more realistic models, which often involve a tremendous number of nodes. As a result, there must be some new algorithms, or more powerful hardware, to reduce the computation time to a comfortable level.

In order to have a better representation of the joint, the finite-element programme should be able to model the gliding contact surface and the synovial fluid. In fact, this feature has already been included in many recent finite-element programmes.

For the simulation results presented in this thesis, the frequency of the input stimulus is assumed to be low enough so that the effects of the inertia and damping can be ignored. It would be useful to extend the frequency range. The main challenge here is to estimate the damping coefficients. In addition, the computation time would increase drastically compared with that in a static test. Some work is needed to reduce the simulation time.

## REFERENCES

- Ascenzi A, Bonucci E (1967): "The tensile properties of single osteons" *Anat Rec.* Aug 158(4), 375-86
- Babuska I, Aziz AK (1976): "On the angle condition in the finite element method" *SIAM J. Numer. Anal.* 13, 214-226
- Bathe KJ (1982): "Finite element procedures in engineering analysis" Prentice-Hall, New Jersey
- Békésy GV (1941): "On the measurement of the amplitude of vibration of the ossicles with a capacitive probe" *Akust. Zeitschr*, Vol.6, 1-16 [in German]
- Boubez TI (1986): "Three-dimensional finite-element mesh generation using serial sections" M.Eng. Thesis, McGill University, Montréal.
- Crane Jr. HL, Gibbs NE, Poole Jr. WG, Stockmeyer PK (1976): "Algorithm 508. Matrix bandwidth and profile reduction" *ACM Trans. Math. Software* 2, 375-377, Complete source in "Collected Algorithms" from ACM
- Dankbaar WA (1970): "The pattern of stapedial vibration" *J. Acoust. Soc. Am.*, 48, 1021-22
- Decraemer WF, Khanna SM, Funnell WRJ (1991): "Malleus vibration mode changes with frequency" *Hearing research*, 54, 305-318
- Decraemer WF, Khanna SM, Funnell WRJ (1994): "A method for determining three dimensional vibration in the ear" *Hear. Res.*, 77, 19-37.
- Decraemer WF, Khanna, SM, Funnell WRJ (2000): "Measurement and modelling of the three-dimensional vibration of the stapes in cat" *Proc. Internat. Symp. on Recent Developments in Auditory Mechanics (Sendai, Japan, 1999 July)*, World Scientific Pub., US, UK, Singapore, 36-43

Elices M (2000), "Structural Biological Materials". Pergamon, Amsterdam, xv+361 pp.

Fried I (1972): "Condition of finite element matrices generated from nonuniform meshes", AIAA Journal 10, pp.219-221

Freitag LA, Ollivier-Gooch (1997): "Tetrahedral mesh improvement using swapping and smoothing" International Journal for Numerical Methods in Engineering, v 40, 3979-4002

Funnell SM (1989): "An approach to finite-element modeling of the middle-ear" M.Eng. Thesis, McGill University, Montréal

Funnell WRJ (1972): "The acoustical impedance of the guinea-pig middle ear and the effects of the middle-ear muscles", M.Eng. Thesis, McGill University, Montréal

Funnell WRJ (1975): "*A theoretical study of eardrum vibrations using the finite-element method*" Ph.D. Thesis, McGill University, Montréal

Funnell WRJ, Laszlo CA (1978): "Modeling of the cat eardrum as a thin shell using the finite-element method" J. Acoust. Soc. Am., 63, 1461-1467

Funnell WRJ, Laszlo CA (1982): "A critical review of experimental observations on ear-drum structure and function" ORL, 44, 181-205

Funnell WRJ (1983): "On the undamped natural frequencies and mode shapes of a finite-element model of the cat eardrum" J. Acoust. Soc. Am., 73, 1657-1661

Funnell WRJ, Decraemer WF, Khanna SM (1987): "On the damped frequency response of a finite-element model of the cat eardrum" J. Acoust. Soc. Am., 81, 1851-1859

Funnell WRJ, Khanna SM, Decraemer WF (1992): "On the degree of rigidity of the manubrium in a finite-element model of the cat eardrum" J. Acoust. Soc. Am., 91, 2082-2090

Funnell WRJ (1996a): "Finite-element modelling of the cat middle ear with elastically suspended malleus and incus" 19th Midwinter Res. Mtg., Assoc. Res. Otolaryngol., St. Petersburg Beach

Funnell WRJ (1996b): "Low-frequency coupling between eardrum and manubrium in a finite-element model" J. Acoust. Soc. Am., 99, 3036-3043

Funnell WRJ, Decraemer WF (1996): "On the incorporation of moiré shape measurements in finite-element models of the cat eardrum" J. Acoust. Soc. Am., 100, 925-932

Fung YC (1993): "Biomechanics, mechanical properties of living tissues" Springer-Verlag, 466-499

George PL, Seveno E (1994): "The advancing-front mesh generation method revisited" International journal for numerical methods in engineering, Vol. 37, N. 21, 3605-3619

Ghosh SS (1996): "On the effects of incudostapedial joint flexibility in a finite-element model of the cat middle ear" M. Eng. Thesis, McGill University, Montréal

Ghosh SS, Funnell WRJ (1995): "On the effects of incudostapedial joint flexibility in a finite-element model of the cat middle ear" Engineering in Medicine and Biology Society, 1995., IEEE 17th Annual Conference , Vol. 2, 1437 -1438

Guinan JJ, Peake WT (1967): "Middle-ear characteristics of anesthetized cats" J. Acoust. Soc. Am., 41, 1237-1261

Gundersen T, Hogmoen K (1976): "Holographic vibration analysis of the ossicular chain" Acta Otolaryngol. (Stockholm), 82, 16-25

Gyo K, Aritomo H, Goode RL (1987): "Measurement of the ossicular vibration ratio in human temporal bones by use of a video measuring system" Acta Otolaryngol. (Stockholm), 103, 87-95.

Helmholtz HLF (1869): "The mechanism of the middle-ear ossicles and of the eardrum" Pflügers Archiv. F. Physiol. (Bonn) 1, 1-60 [in German: trnas, by Buck AH and Smith N (Wood W, New York, 1873 69 pp.) and by Hinton J, (Publ. New Sydenham Soc. London 62, 97-155 (1874).

Hewitt JD, Glisson RR, Guilak F, Vail TP (2001): "Regional materials properties of the human hip capsule ligaments" J Ortho Res, 19(3):359-364

Hüttenbrink K-B (1997): "The middle ear as a pressure receptor",. Proceedings of Middle ear mechanics in Research and Otolaryngology, Dresden, 15-20

Itoi E, Kuechle DK, Newman SR (1993): "Stabilising function of the biceps in stable and unstable shoulders" J Bone Joint Surg Br. 75(4), 546-550

Jayne H (1898): "Mammalian anatomy" I. The skeleton of the cat. (Lippincott, Philadelphia)

Khanna SM, Tonndorf J (1972): "Tympanic membrane vibrations in cats studied by time-averaged holography" J. Acoust. Soc. Am., 51, 6, 1904-1920

Khanna SM, Decraemer WF (1996): "Vibrations modes and the middle ear function" Proceedings of Middle ear mechanics in Research and Otolaryngology, Dresden, 21-26

Ladak HM (1993): "Finite-element modelling of middle-ear prosthesis in cat" M.Eng. thesis, McGill University, Montréal

Ladak HM, Funnell WRJ (1994): "Finite-element modelling of malleus-sapes and malleus-footplate prostheses in cat" 17<sup>th</sup> Midwinter Res. Mtg., Assoc. Res. Otolaryngol., St. Petersburg Beach

Lim DJ (1968): "Tympanic membrane. Electron microscope observation. Part I. Pars tensa" Acta Otolaryngol., Vol. 66, 181-198

Lynch TJ, Nedzelitsky V, Peake WT (1982): "Input impedance of the cochlea in cat", J. Acoust. Soc. Am., Vol. 72, 108-130

Mente PL, Lewis JL (1994), "Elastic modulus of calcified cartilage is an order of magnitude less than that of subchondral bone", J. Orthop. Res. 12: 637

Moller P, Hansbo P (1995): "On advancing front mesh generation in three dimensions" International journal for numerical methods in engineering, Vol. 38, N. 21, 3551-3568

Murray RP, Hayes WC, Edwards WT, Harry JD (1984), "Mechanical properties of the subchondral plate and the metaphyseal shell", Trans. Orthop. Res. Soc. 9: 197

Nager GT, Nager M (1953): "The arteries of the human middle ear, with particular regard to the blood supply of the auditory ossicles", Ann. Otol. Rhinol. Laryngol. Vol. 62, 923-949

Nigg BM, Herzog W (1999): "*Biomechanics of the musculo-skeletal system 2<sup>nd</sup> edition*" Wiley 1999

Ollivier-Gooch CF (1998): "An unstructured mesh improvement toolkit with application to mesh improvement, generation and (de-)refinement" Presented at the AIAA 36<sup>th</sup> Aerospace Sciences Meeting, Reno, Nevada, January 1998. AIAA 98-0218

Palchun VT, Magomedov MM (1997): "Some anatomical features of the long process of the incus" Bulletin of otorinilaringology, No.2

Rho JY, Tsui TY, Pharr GM (1998): "Elastic properties of osteon and trabecular bone measured by nanoindentation" J. Biomed. Mater. Res. 45, 48-54.

Shewchuk JR (1998): "Tetrahedral Mesh Generation by Delaunay Refinement" Proceedings of the Fourteenth Annual Symposium on Computational Geometry (Minneapolis, Minnesota), 86-95

Tonndorf J, Khanna SM (1970): "The role of the tympanic membrane as a part of the middle ear transformer" Acta Otolaryng., Vol. 71, 177-180

Von Békésy G (1960): "*Experiments in Hearing*" New York: McGraw-Hill

Wada H, Metoki T, Kobayashi T (1992): "Analysis of dynamic behavior of human middle ear using a finite-element method" J. Acoust. Soc. Am., 96, 3157-3168

Wolff D, Bellucci RJ, Eggston AA (1957): "Microscopy anatomy of the temporal bone" Williams & Wilkins, Baltimore: ix + 414 pp

Yuan JS, Fitzsimons CJ (1993): "A mesh generator for tetrahedral elements using Delaunay triangulation" IEEE Transaction on magnetics, vol. 29, 1906-09